

Project thesis

Automated clocked dynamics in a pinwheel ASI

Eivind Heggelund

Supervisor Erik Folven
Co-supervisors: Ida Breivik
 Dheerendra Singh Bhandari

December 19, 2023

Abstract

Artificial Spin Ice (ASI) is a type of magnetic metamaterial utilizing an array of interacting nanomagnets. These interactions lead to fascinating phenomena, which has shown promise for use in unconventional computing.

For this project, a magneto-optical Kerr effect (MOKE) microscope, which is used to perturb and image ASIs, has been successfully automated. The implementation was done by expanding the existing software controlling the instrument, allowing access to its functionality by writing commands in a text script. The implementation also includes methods for the post processing of images to acquire magnetization data.

To evaluate the success of the implementation, measurements were obtained performing automated astroid clocking on a 45° pinwheel ASI. Discrete magnetic field pulses with a constant field strength were applied along $\pm 22^\circ$ alternatingly to achieve growth of magnetic domains, followed by clocking along $\pm 158^\circ$ to reverse the growth. The measurements substantiated the presented theory well, indicating that the implementation works as intended.

Alternated clocking pulses were shown to be the driver behind the domain growth, as little to no growth was observed for the unidirectional clocking. Time series and plots illustrating the time evolution of the ASIs during repeated clocking sequences showed a high degree of reproducibility, both in the total magnetization and the spacial distribution. Growth was seen to initiate in the same few, seemingly random, regions of the sample, suspected to be caused by small defects. The results indicated that the fabrication of patterned defaults in the ASIs might serve as a way to control where growth is initialized in the future, as well as being promising for the use of ASIs for unconventional computing.

Image processing was performed to correct for an observed drift in brightness over the image stack using a reference box outside the ASI. The correction worked well, but were unable to remove all of the drift from the images. Pixel values were converted to plots of magnetization, using pixel values from images taken of the ASIs polarized along 0° and 180° for calibration. Due to the uncorrected drift in brightness, the magnetization was not always contained by the calibration values. Another method to calibrate the data was explored using thresholding. The thresholding seemed promising, but further exploration into the removal of noise from the image data is required for it to work properly.

The automation opens many possibilities for future work and exploration, such as testing using more complex clocking cycles, and different types of structures and geometries.

This work is licensed under CC BY-NC 4.0

Acknowledgements

I would like to thank my supervisors, Erik Folven, Ida Breivik and Dheerendra Singh Bhandari for all the guidance, discussions and feedback received during this semester, as well as entrusting me with their new and expensive equipment. I would also like to thank Ivan Soldatov at Evico Magnetics for supplying the source code and providing LabView support.

Contents

1	Introduction	1
2	Theory	3
2.1	Magnetism	3
2.1.1	Dipole model and interactions	3
2.1.2	Magnetization and ordering	4
2.1.3	Ferromagnetic materials	5
2.2	Artificial Spin Ice	7
2.2.1	Astroid clocking	8
2.3	Magneto-optical Kerr effect (MOKE)	10
3	Characterization tools and software	11
3.1	MOKE microscope	11
3.2	LabView	13
4	Experimental procedure	14
4.1	LabView programming	14
4.1.1	Source code	14
4.1.2	Scripting	16
4.2	Testing	18
4.3	Image processing and plotting	19
5	Results and discussion	20
5.1	Scripting FP	20
5.2	Image processing	20
5.3	Automated astroid clocking	24
5.3.1	Hysteresis	24
5.3.2	Clocking at 30 mT, 32 mT and 33 mT	25
5.3.3	Comparison of manual, automated and reference clocking	25
5.3.4	Unidirectional clocking	26
5.3.5	Multiple automated runs	27
5.3.6	Validation of image processing	30
6	Conclusion and outlook	33
A	Scripting	35
A.1	AB ab script	35
A.2	Script commands	37
A.3	AB ab clocking	38

Chapter 1

Introduction

There is an ever-growing need for computing power in the world today. Unfortunately, the generation of this computing power doesn't come for free. Estimates shows that the global Information and Communication Technology (ICT) ecosystem accounted for between 4% to 6% of the total electricity consumption in 2020, with consumption expected to increase further over the coming decades [1].

One solution to this issue involves a continuation of the improvements in efficiency achieved within conventional transistor technology. However, this technology is reaching the atomic scale, making further down-scaling and improvements problematic [2]. Consequently, there is a need for new computing methods accommodating both the energy and computation challenges the world is facing.

Another possible solution involves the utilization of single-domain nanomagnets as information carriers. Since these magnets can be fabricated with binary magnetization states, it makes them ideal to represent single bits in computation, and isolated single-domain nanomagnets are already in used for conventional magnetic storage [3]. While this has proved successful, many interesting properties can be obtained by allowing the nanomagnets to interact with each other. Since magnets don't communicate using a dissipative flow of electrons, but rather through magnetic interactions, its use can constitute a huge improvement in energy efficiency.

Artificial Spin Ice (ASI) is a type of magnetic metamaterial, utilizing an array of interacting nanomagnets. The close proximity of the magnets leads to interactions which leave some magnets geometrically frustrated, resulting in emergent properties not observed in individual nanomagnets. These frustrations allow for many different magnetization states, which can be utilized for new low-energy computational devices [4, 5].

A lot of progress have been made within this field through the last decades, but large parts still remains unexplored, and no functioning full-scale applications using ASI-based computation have yet been realized [5]. The progress achieved is a combination of theoretical derivations, computer simulations and experimental work. A key factor, especially for the experimental work, is the ability to obtain large amounts of useful data to verify the validity of the results. The automation of the experimental setup might be of huge assistance to this end.

The aim of this project was to successfully automate a magneto-optical Kerr effect (MOKE) microscope, which is used to perturb and image ASIs. The implementation also includes methods for the post processing of images to acquire magnetization data. To evaluate the success of the implementation, automated astroid clocking was performed, based on a method described in a paper by Jensen and Strømberg [6], as it utilizes a lot of the features implemented, is quite repetitive and somewhat time consuming.

Outline

This thesis will begin by establishing the theoretical background of magnetism, ASIs and magneto-optics in Chapter 2. Chapter 3 will cover the characterization tools and software which are to be automated. The experimental procedure, both covering the automation and measurements done to verify it, is explained in Chapter 4. Chapter 5 will present the results of the project and discuss them, both the finished automation and the experimental measurements. Lastly, Chapter 6 will present a conclusion and outlook for the project.

Chapter 2

Theory

This chapter will cover the theoretical foundation needed to understand Artificial Spin Ice, how they behave and how they can be investigated. Section 2.1 covers general concepts of magnetism, beginning with the dipole model and the various interactions that determine its behaviour. Then, ordering of dipoles into magnetic domains will be discussed, after which a more in-depth exploration of ferromagnetic materials and their properties will be presented. This will bring us over to Section 2.2, where Artificial Spin Ice will be covered, including an introduction of the theory behind astroid clocking. Finally, Section 2.3 will cover the magneto-optical Kerr effect, which is necessary to understand the instrument used.

The theoretical background and equations are based on *Magnetism and magnetic materials* by J.M.D. Coey [3] and *Magnetic materials - Fundamentals and applications* by N. A. Spaldin [7], unless otherwise stated.

2.1 Magnetism

Magnetism describes the physical phenomena where the motion of electric charges cause objects to attract or repel each other. It shares many similarities with the electrostatic forces between electrically charged particles, and the two effects are closely linked. For this reason, we often combine magnetism and electrostatics into the area of physics we call electromagnetism.

The foundation for our understanding of electromagnetism is Maxwell's equations. The second of these equations,

$$\nabla \cdot \mathbf{B} = 0, \quad (2.1)$$

states that the magnetic flux density \mathbf{B} is free from divergence. From this follows the impossibility of a material to only serve as a source or sink for a magnetic field, which is called a monopole. This differs greatly from the electrostatic effect, where a charged particle can produce electric fields that only radiate either outwards or inwards.

2.1.1 Dipole model and interactions

In the magnetic dipole model, magnets are visualized with two poles, with magnetic field lines enveloping the magnet from north to south pole, and a magnetic moment \mathbf{m} closing the loop from south to north.

The magnetic moment can be described in two ways. Firstly, viewing it from the point of a current loop yields $\mathbf{m} = I\mathbf{A}$, with circulating current I and vector area \mathbf{A} . This description is particularly useful with regard to electromagnets. Secondly, viewing it as two magnetic poles with strengths $\pm p$ and separation \mathbf{r} yields $\mathbf{m} = p\mathbf{r}$.

The behaviour of individual magnetic dipoles is driven towards the minimization of the total energy of the system. The main contributions to this energy are exchange interactions, thermal energy, interactions with external fields, and dipole interactions.

Exchange interactions

The quantum origins of magnetism is predominantly connected to the electron angular momentum, which is caused by both orbital motion of the electron around the nucleus \mathbf{l} and its intrinsic spin \mathbf{s} . Both contributions of the angular momentum are directly proportional to the magnetic moment through its corresponding gyromagnetic ratio γ_i , with formulas $\mathbf{m}_l = \gamma_l \mathbf{l}$ and $\mathbf{m}_s = \gamma_s \mathbf{s}$.

The electron spins give rise to an exchange interaction given by

$$E_{\text{exch}} = -2J\mathbf{S}_i \cdot \mathbf{S}_j, \quad (2.2)$$

where \mathbf{S}_i and \mathbf{S}_j are the total electron spin from two neighbouring atoms. The exchange constant J can be both positive and negative depending on the material. A positive J favors the alignment of neighbouring spins in the same direction, while a negative J favors an antiparallel alignment.

Temperature

The thermal energy is given by

$$E_T = k_B T, \quad (2.3)$$

with temperature T in Kelvin and Boltzmann's constant k_B equaling $1.3807 \times 10^{-23} \text{ J K}^{-1}$. Thermal energy doesn't favor any particular direction of magnetic moments, but cause unordering of the system by orienting magnetic moments in random directions.

External fields and dipole interactions

The potential energy of a magnetic dipole in an external magnetic field \mathbf{H} , also known as the Zeeman energy, is given by

$$E_{\text{Zee}} = -\mu_0 \mathbf{m} \cdot \mathbf{H}, \quad (2.4)$$

with the vacuum permeability μ_0 equaling $4\pi \times 10^{-7} \text{ N A}^{-2}$. $|E_{\text{Zee}}|$ is maximized when $\mathbf{m} \parallel \mathbf{H}$, and the negative sign causes it to favor the alignment of the magnetic dipole moment with the external magnetic field.

Similarly, two dipole moments will interact with the stray field set up by the other with an interaction energy given by [8]

$$E_{\text{dip}} = -\frac{\mu_0}{4\pi} \left(\frac{3(\mathbf{m}_1 \cdot \mathbf{r})(\mathbf{m}_2 \cdot \mathbf{r})}{|\mathbf{r}|^5} - \frac{\mathbf{m}_1 \cdot \mathbf{m}_2}{|\mathbf{r}|^3} \right), \quad (2.5)$$

where \mathbf{r} denotes the vector separating the dipole moments \mathbf{m}_1 and \mathbf{m}_2 . E_{dip} also favors the alignment of dipoles in the same direction.

2.1.2 Magnetization and ordering

The relative strengths of the mentioned energy contributions are material dependent, and give rise to ordering of dipoles into different types of domains. For the types we will cover placed at room temperature, the Zeeman energy always dominates when a sufficiently strong external field is applied. Hence, the domain classifications will assume that no external field is

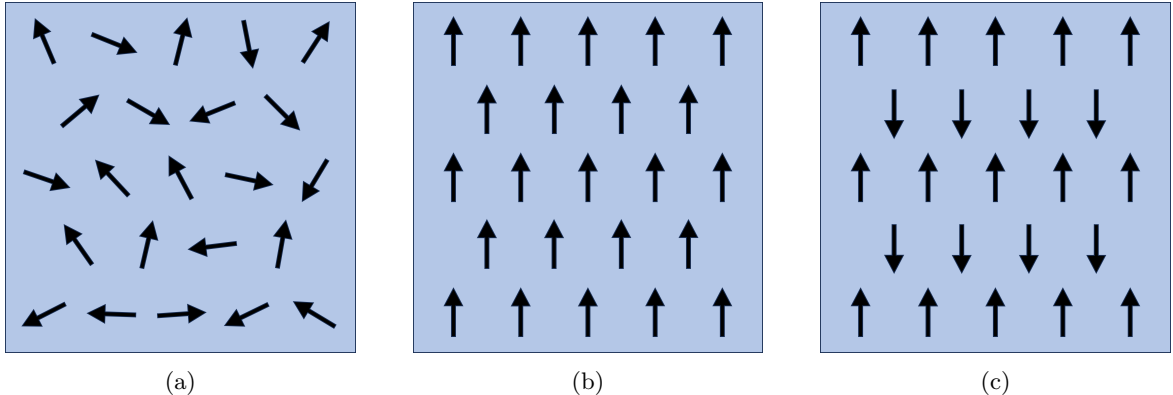


Fig. 2.1: Magnetic moments visualized for three different domain types at room temperature without an external field applied. (a) Paramagnetic material with random orientations. (b) Ferromagnetic material with unidirectional orientation. (c) Antiferromagnetic material with antiparallel orientation.

applied. Dipole interactions are the weakest of the terms at room temperature, but becomes more important at lower temperatures.

For paramagnetic materials, the thermal energy term dominates, causing the dipoles to orient themselves in random directions. Exchange interactions dominate for ferromagnetic and antiferromagnetic materials, with J being positive and negative respectively, leading to parallel and antiparallel ordering. The magnetic moments of the three domain types are visualized in Fig. 2.1.

In many applications, such as Artificial Spin Ice, we are more interested in the total magnetic moment of a larger part of the material than individual dipoles. Hence, we define a magnetization within a given volume V as

$$\mathbf{M} = \frac{\sum_V \mathbf{m}}{V}. \quad (2.6)$$

While paramagnetic and antiferromagnetic domains have zero net magnetization without the presence of an external field, caused by the magnetic moments canceling each other out, ferromagnetic domains have a non-zero magnetization which will be utilized further.

2.1.3 Ferromagnetic materials

Stray fields and domain boundaries

Samples that are small enough in size, more specifically below the single domain limit, contain one unidirectional domain. However, larger samples will contain a patchwork of domains pointing in different directions. This is caused by the minimization of the magnetostatic energy related to the stray field, which is given by

$$E_d = -\frac{\mu_0}{2} \int \mathbf{H}_d \cdot \mathbf{M} dV, \quad (2.7)$$

where \mathbf{H}_d is the stray field generated by the sample and V denotes a given volume. The energy favors smaller \mathbf{H}_d , which the sample achieves either by splitting single domains into multiple, as visualized in Fig. 2.2a-c, or by aligning the magnetization along its easy axis, as opposed to its hard axis as visualized in Fig. 2.2d.

Hard and easy axes are determined by the geometry of the sample, with the easy axis extending parallel to the longest dimension of the sample and the hard axis parallel to the shortest. Consequently, utilizing anisotropy provides an effective way of controlling the magnetization axis of our structures.

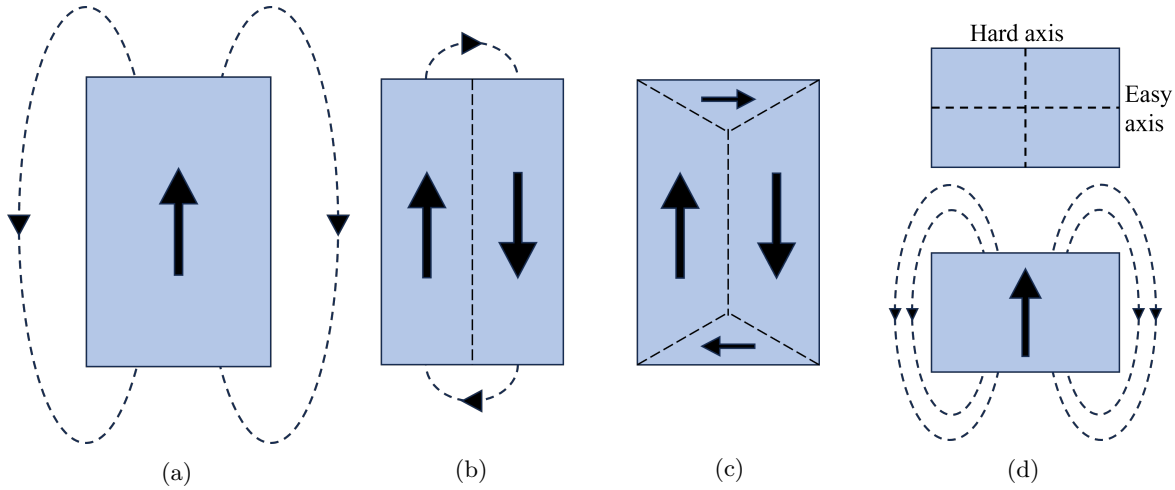


Fig. 2.2: Visualization of the reduction of stray fields generated by a magnet by domain formation or axis reorientation. This leads to a minimization of the magnetostatic energy of the sample. (a) Single domain with magnetization along its easy axis, generating a large stray field. (b) Splitting of single domain into two domains, causing a decrease in the stray field. (c) Flux-closure domain structure with zero stray fields or magnetostatic energy. (d) Hard and easy axes are indicated for a rectangular structure. Magnetization oriented along the hard axis creates the largest stray field, and is not favored.

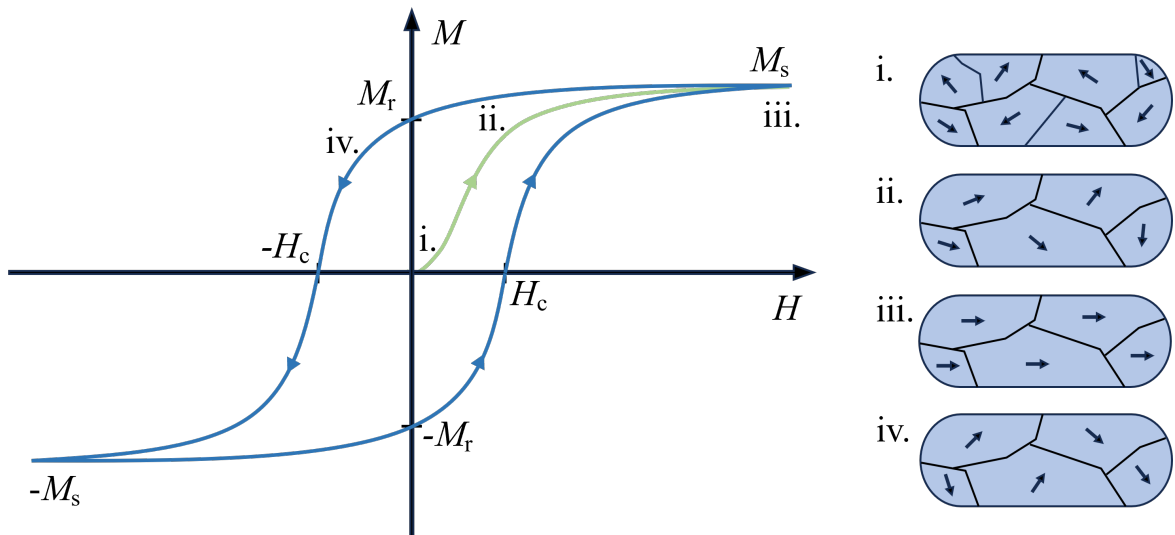


Fig. 2.3: Hysteresis curve for ferromagnetic materials. i. Before an external field is applied, the material contains no net magnetization. ii. An external field is applied along positive x-axis, causing domains to start aligning and combining. iii. For a sufficiently strong external field, all domains align with the field, giving a maximum saturation magnetization of strength M_s . iv. Material keeps its positive magnetization even for a small external field along negative x-axis, provided this field is weaker than the coercive field H_c .

Hysteresis

A key property of ferromagnetic materials is that they undergo hysteresis, as seen in Fig. 2.3. Before being exposed to an external field, the ferromagnetic material has zero net magnetization, caused by the mentioned stray field minimization. When applying an external field of strength H along positive x-axis, domains start to align and combine. For a sufficiently strong external field, all magnetization will be aligned with the external field, summing up to a maximum saturation magnetization of strength M_s . Subsequently, if the external field is turned off, the material will still conserve a positive net magnetization of strength M_r . The positive net magnetization is retained, even for a small field applied along negative x-axis, provided the field is weaker than the coercive field H_c . These properties serve as a type of memory, as the material can remember previously applied fields through its magnetization.

2.2 Artificial Spin Ice

The concept of Artificial Spin Ice (ASI) was introduced by Wang et al. [4] in 2006, in an attempt to mimic the frustration of hydrogen ion positions in frozen water using geometrically frustrated two-dimensional magnetic lattices. The reason why these frustrations are interesting to investigate, lies in how they allow for many different equilibrium configurations depending on the initialization of the system. In the 17 years following its conception, many further advances have been made, with ASIs yielding promising results for the use as reprogrammable magnonic crystals [5].

The individual magnets in ASIs are made of ferromagnetic materials, utilizing many of the previously mentioned properties. The magnets have sizes below the single domain limit, and are elongated in one direction to control the direction of the magnetization. Typical dimensions used are $220 \text{ nm} \times 80 \text{ nm}$ and shaped like a stadium. The two-dimensional geometry allows for easier probing of the structure, especially compared to bulk structures.

There exists infinitely many ASI structures and geometries to be explored, but we will mainly concern ourselves with square and pinwheel, as shown in Fig. 2.4. Different pinwheel structures are differentiated by the indicated angle θ , with magnets being rotated by $\pm\theta$.

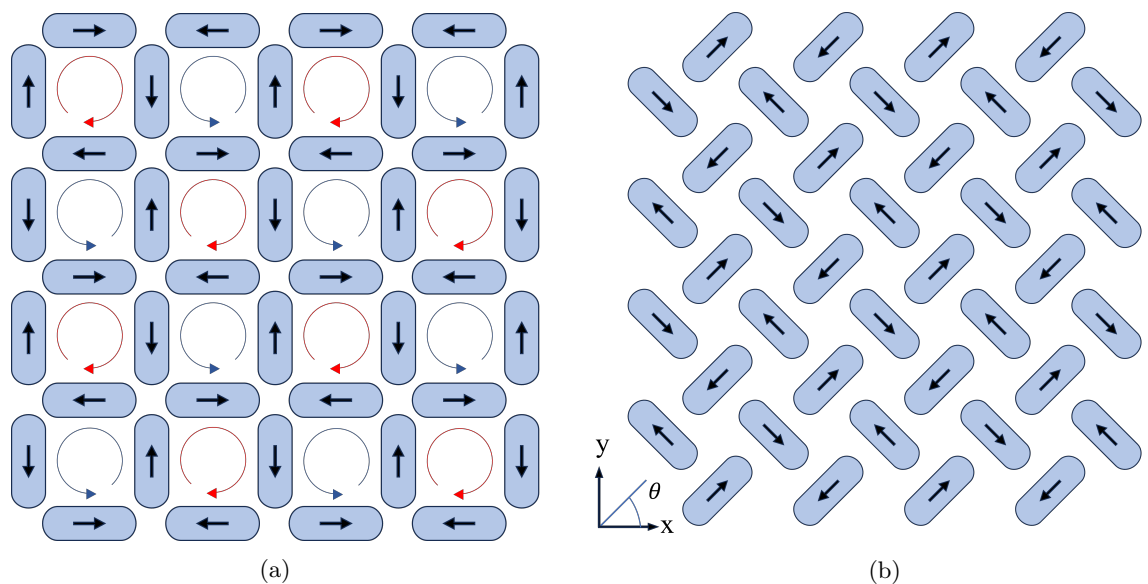


Fig. 2.4: (a) Square ASI in ground state. (b) Pinwheel ASI oriented along $\pm 45^\circ$ in ground state.

2.2.1 Astroid clocking

One of the current issues with ASIs has been the lack of complex and efficient protocols to control the state evolution of the system. This issue is addressed in a paper by Jensen and Strømberg et al. [6], where they introduce *astroid clocking* as a procedure to control the growth and reversal of magnetic domains.

The procedure utilizes a global field, which is applied to the whole ensemble of magnets. What separates this procedure from various previous approaches is the use of field angles to modulate the behavior of the system, contrary to using field strengths. The issue with field strength modulation is the hysteresis-like nature of ferromagnetic materials, causing avalanches of flipping which are hard to control [9]. With field angle modulation, it is possible to only modify a desired part of the ensemble.

The magnetic behavior during astroid clocking can be understood in the light of the Stoner-Wohlfarth model, which describes the minimal external field \mathbf{H} needed to orient a single-domain magnet along any arbitrary angle [10]. The field is modelled by the astroid equation

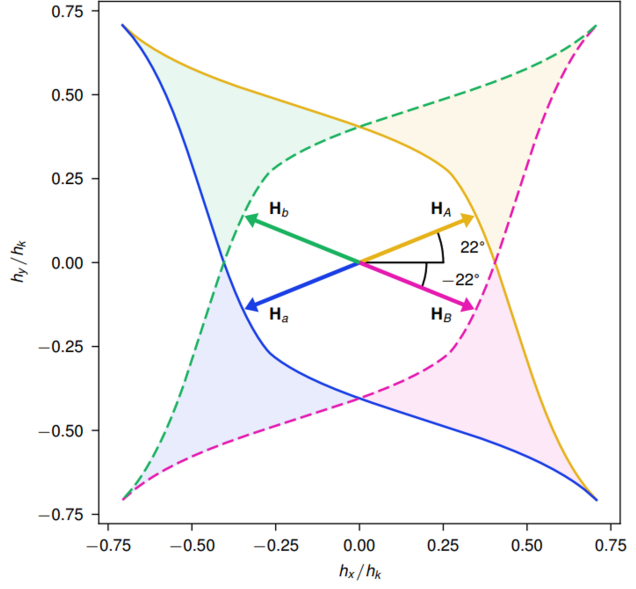
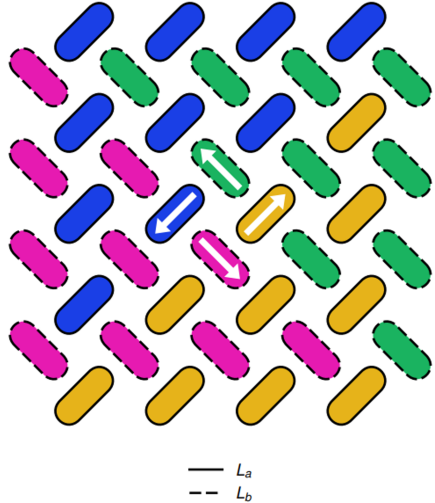
$$\left(\frac{H_{\perp}}{H_K}\right)^{2/3} + \left(\frac{H_{\parallel}}{H_K}\right)^{2/3} = 1, \quad (2.8)$$

where H_{\perp} and H_{\parallel} are the components of \mathbf{H} along the hard and easy axes respectively, and H_K describes the coercive field along the hard axis. The switching astroid is plotted for the two types of magnet rotations in a 45° pinwheel structure in Fig. 2.5a, with magnets oriented along $+45^{\circ}$ being denoted as sublattice L_a with solid outlines and magnets oriented along -45° as sublattice L_b with dashed outlines. Four colored regions can be observed in the astroid plot, corresponding to the four different magnetization orientations indicated in the ASI. Fields associated with these areas will exclusively promote switching of magnets in one of the sublattices. E.g. a field corresponding to the yellow area will be strong enough to switch the orientation of magnets in L_a along its easy axis, but not magnets in L_b along its hard axis.

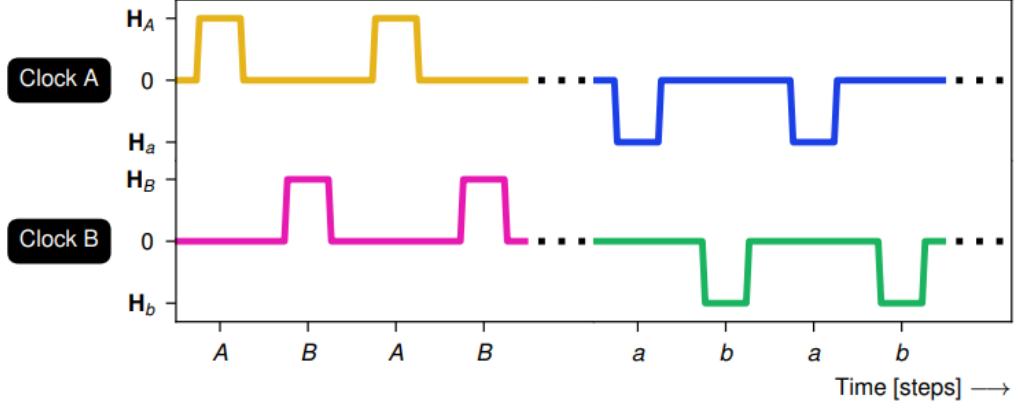
If a field is chosen on the border of the astroid plot, the behaviour of each magnet will be determined by the dipole fields exerted by its neighbours. A magnet located in the middle of a domain will feel a strong dipole field from its neighbours, changing the total perceived field and preventing flipping. This, combined with an alternating pattern of L_a and L_b sublattices, results in a stepwise growth of domains, only occurring along existing domain borders.

The four clock fields we will utilize are also visualized in Fig. 2.5a, denoted as \mathbf{H}_A , \mathbf{H}_B , \mathbf{H}_a and \mathbf{H}_b . The fields are oriented along $\pm 22^{\circ}$ with respect to the x-axis, as these are the angles within the colored areas with the minimum required field strength. In astroid clocking, two or more of these clock fields will be applied in turn as discrete pulses, as visualized in Fig. 2.5b. For an ASI initially polarized along 180° , containing only blue and green orientation, an alternating clocking of \mathbf{H}_A and \mathbf{H}_B (simply denoted as AB-clocking) will cause growth of yellow and pink domains, while clocking of \mathbf{H}_a and \mathbf{H}_b (denoted as ab-clocking) will reverse the growth.

It is observed an asymmetry in the ways domain growth and reversal proceeds, with domains mainly growing horizontally from the vertical edges, while reversal happens in both vertical and horizontal directions. This leads to the reversal being much faster than the initial growth.



(a)



(b)

Fig. 2.5: (a) A 4×4 pinwheel ASI and its corresponding switching astroids, with magnets oriented along $+45^\circ$ denoted as sublattice L_a with solid outlines and -45° as sublattice L_b with dashed outlines. Four clock fields are indicated as \mathbf{H}_A , \mathbf{H}_B , \mathbf{H}_a and \mathbf{H}_b , each inside one of the colored areas that exclusively promotes reorientation of magnets in one type of sublattice. (b) Visualization of the discrete clock pulses. AB-clocking will be used to grow domains, while ab-clocking will reverse them. Figures used with permission from Jensen and Strømberg et al. [6].

2.3 Magneto-optical Kerr effect (MOKE)

Magneto-optics describes various phenomena where photons interact with magnetically polarized materials. One of these phenomena is the Magneto-optical Kerr effect (MOKE), which occurs for photons that are reflected from the surface of a magnetic material, leading to a change in the photon polarization or reflectance proportional to the magnetization of the material.

The MOKE can be observed through three different experimental geometries, but this work has mainly utilized the longitudinal geometry. The setup is visualized in Fig. 2.6. For this geometry, either *s*- or *p*-polarized light is applied with a plane of incidence parallel to the direction of the magnetization we want to observe [11]. The interaction with the magnetization causes both a rotation of the polarization by angle θ_k and an ellipticity. The elliptical polarization can be removed with a compensator, leaving a linearly polarized light that can be compared with the original polarization to obtain θ_k . θ_k is typically in the order of 0.1°. The proportionality between θ_k and the magnetization can be exploited to characterize magnetic samples.

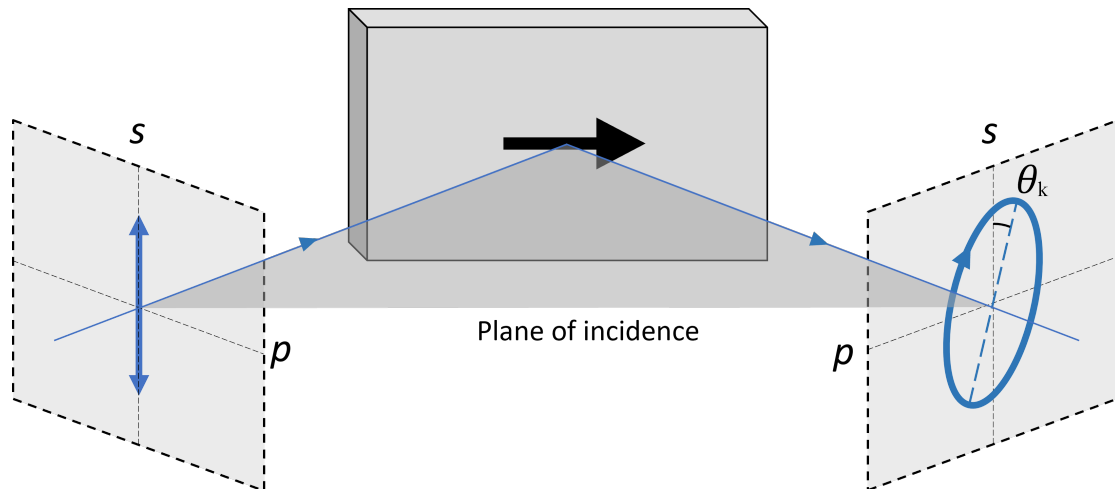


Fig. 2.6: Visualization of the MOKE using longitudinal geometry. An initial *s*-polarization is shown, but *p*-polarization is also possible to use. The main property of interest is θ_k , which is proportional to the magnetization of the sample. Note that the rotation is greatly exaggerated in the figure, and is typically in the order of 0.1°.

Chapter 3

Characterization tools and software

3.1 MOKE microscope

The MOKE microscope utilizes the magneto-optical Kerr effect for real-time characterization of the magnetic properties of the surface of a material. In combination with external electromagnets, it can be used to investigate the time evolution of the magnetization of the sample. The experimental setup is visualized in Fig. 3.1. The microscope in use is well described in a paper by Soldatov and Schäfer [12], which alongside the manual for the microscope serves as the reference for the specifications given in this section, unless otherwise stated.

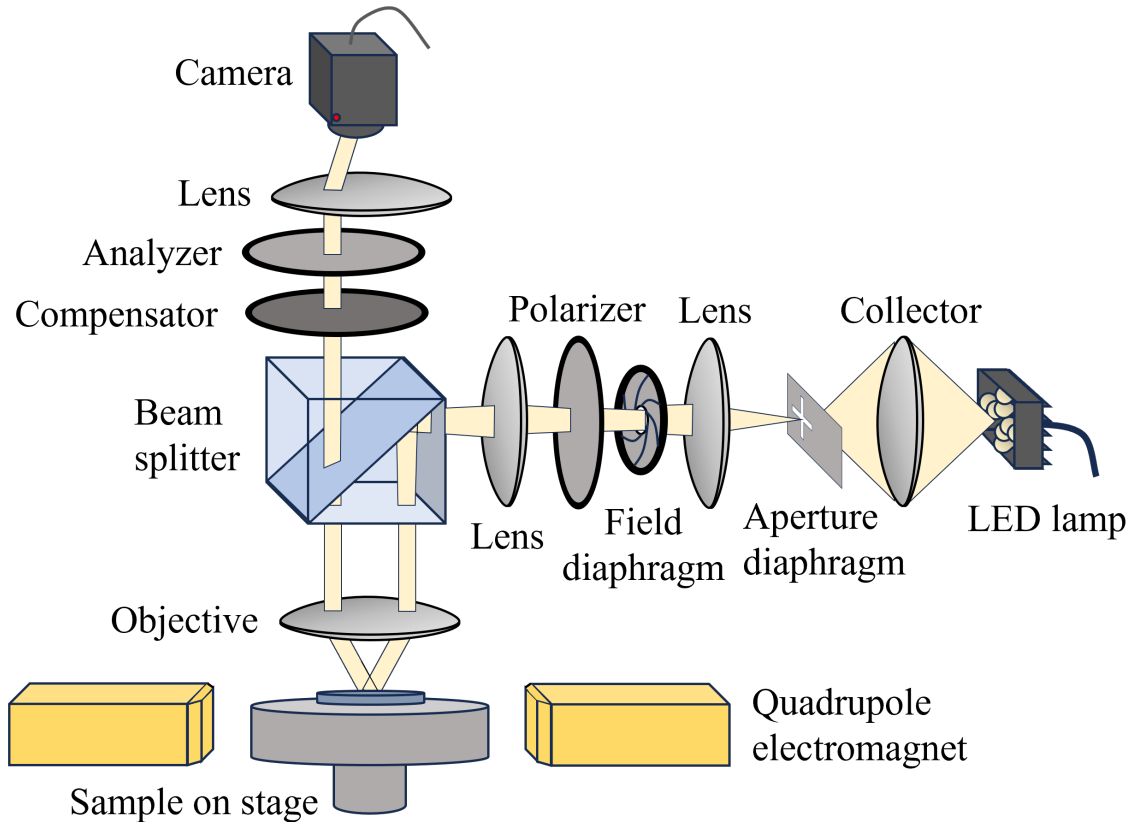


Fig. 3.1: A schematic representation of the main components of the MOKE microscope.

The MOKE microscope utilizes a setup with 8 LEDs as the illumination source, organized in a cross pattern and indexed from 1 to 8 as visualized in Fig. 3.2a. Whereas conventional microscopes using a single illumination source utilize apertures for control of the incident angles, and by extension the experimental geometry, the same can be achieved by simply turning on or off LEDs. The difference is visualized for the 8 LED design and the conventional single source setup in Fig. 3.2a-b.

Turning on LEDs 1 and 2 will image using the longitudinal MOKE geometry, with magnetic contrast along the vertical direction of the image, as well as some polar contrast. Turning on LEDs 5 and 6 will also image using longitudinal geometry, but with contrast in transverse and polar direction. Turning on LEDs 7 and 8 is equivalent to 5 and 6, only with inverted contrast in the transverse direction.

The use of LEDs also enables strobe lighting, opening up various possibilities for contrast enhancement. Alternately strobing LEDs 1 and 2 followed by 5 and 6, allows for practically simultaneous imaging with both vertical and transverse contrast. Strobing LEDs 5 and 6 followed by 7 and 8, and summing the two images removes the vertical contrast and enhances

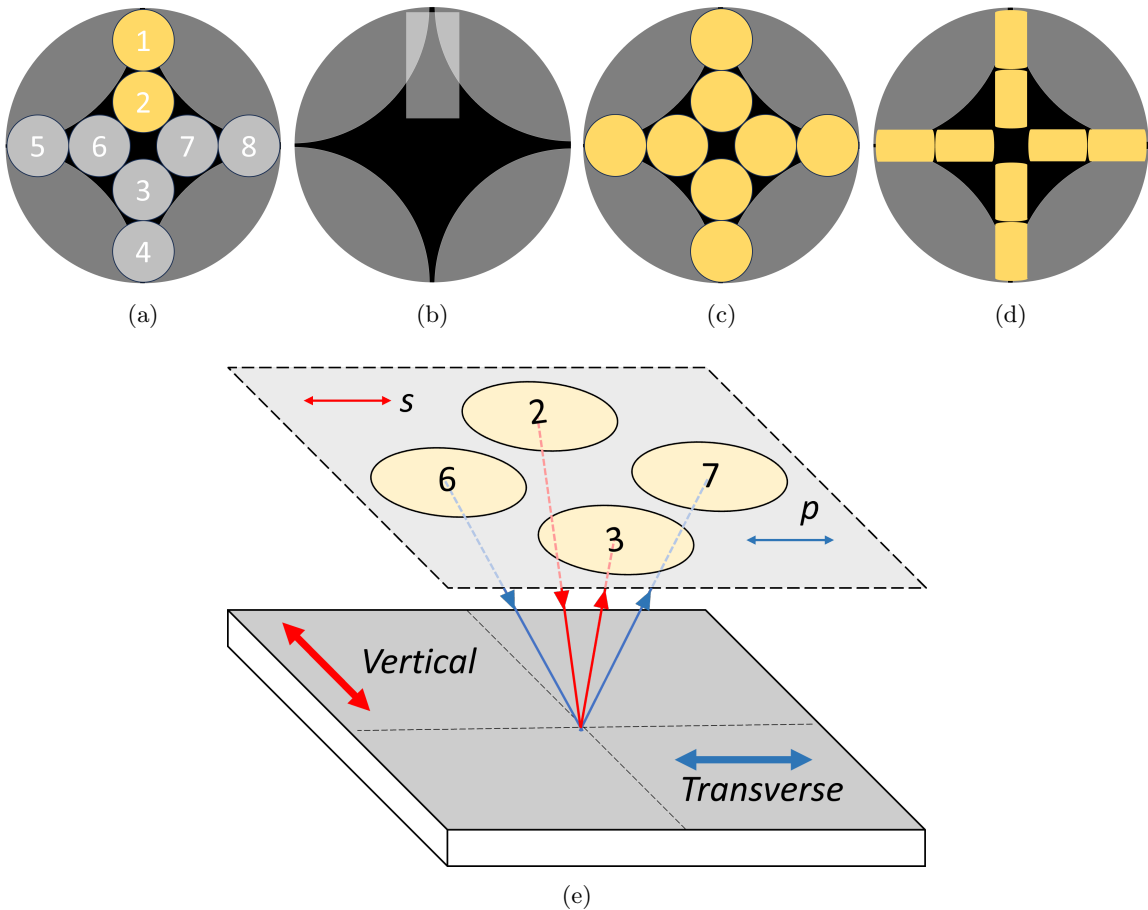


Fig. 3.2: (a) Setup of the 8 LEDs used as the illumination source. With LEDs 1 and 2 turned on, an image with the longitudinal MOKE geometry is obtained, with magnetic contrast along the vertical direction of the image. (b) Aperture placement for setup with single illumination source, achieving the same as the setup in (a). (c-d) Illumination spots before and after the light passes through the cross aperture diaphragm respectively. (e) Light from LEDs 2 and 3, and LEDs 6 and 7, have planes of incidence along the vertical and transverse direction of the sample respectively, allowing us to image magnetic contrast in either direction. The light moving along the vertical direction is *s*-polarized, while the light moving along the transverse direction is *p*-polarized.

the polar contrast. Subtraction of the images removes the polar components, leaving an enhanced purely transverse contrast.

A cross aperture diaphragm is used to achieve rectangular illumination spots. The spots before and after the aperture is visualized in Fig. 3.2c-d. A second diaphragm called the field diaphragm is used to limit the amount of light entering the microscope.

After passing through the field diaphragm, the light is linearly polarized along the transverse direction using a polarizer, resulting in *s*-polarized and *p*-polarized light for the vertical and transverse directions respectively, as seen in Fig. 3.2e. The light is subsequently reflected off the sample. Depending on the material, the linearly polarized photons may become slightly elliptically polarized by the interaction with the sample, in addition to the Kerr rotation θ_k . The ellipticity is removed using a compensator, leaving a linearly polarized light rotated by θ_k . The beam then passes through an analyzer, which is rotated to match θ_k , producing an image of the domain contrasts. Light that has been rotated by $+\theta_k$ will match the polarization of the analyzer and appear bright in the image, while light rotated by $-\theta_k$ will be slightly absorbed by the analyzer and appear darker. The image can be viewed through either an ocular on the microscope, or through a top mounted camera.

A beam splitter and various lenses are used to guide and focus the light beam. One of these lenses is the objective lens, which can be changed depending on the desired magnification. The highest magnification is 100x and requires oil immersion. For this magnification, we are restricted to the innermost LEDs, namely LEDs 2, 3, 6 and 7, as the close proximity of the objective to the sample requires small angles which can't be achieved using the outermost LEDs.

The sample we want to investigate is placed on a piezo-stabilized stage under the objective. The stabilization uses a reference image to calculate the drift of the live image in all three dimensions, and continuously corrects for it by the use of three piezoelectric elements. A quadrupole electromagnet is placed horizontally around the sample, allowing for an external magnetic field to be applied through the sample from any in-plane direction.

The microscope is controlled from a software called KerrLab on a connected computer, which controls everything from LEDs, magnetic field strength and direction, camera imaging modes, and the piezo-stabilizer.

3.2 LabView

KerrLab is created in LabView. LabView is a graphical programming environment designed for use in engineering instruments and measurements. The software is created by National Instruments, and uses G as a programming language, with a drag-and-drop user interface to select components and virtual wires to connect them. Labview works well for running multiple parallel processes, which is needed when controlling the instruments connected to the microscope, and is compatible with a lot of hardware also designed by National Instruments [13].

LabView programs consist of two main windows. Firstly, a front panel (FP) where buttons, indicators, text boxes, graphs and dials can be placed. The FP serves as a graphical user interface when the program is running. Secondly, a block diagram (BD) where most of the computation and logic is defined. Items in the BD can be connected to the FP to read or write data to the user. It can also read and write to files of various types. The code for both windows is stored as a VI-file.

Chapter 4

Experimental procedure

4.1 LabView programming

4.1.1 Source code

The source code for KerrLab was obtained by courtesy of the producer Evico Magnetics. A schematic of the larger components of the code and how they communicate is shown in Fig. 4.1. The main component of the source code is the KerrLab.VI. Its FP is shown in Fig. 4.2, containing many of the features needed to control the MOKE microscope, as well as enabling access to other FPs. The corresponding BD deals with the initialization and termination of the main program and subprograms, control of the camera, electromagnets and piezoelectric elements, message log, and error handling.

Some functionality has been outsourced to other VIs, which is mainly done for compartmentalization and reusability of code. This functionality is imported into the main VI, allowing the main VI to communicate to the SubVIs. Examples of SubVIs are the Magnetic field control (MFC.VI) which appears in the middle of the main FP, the LED controller window (Fiberlamp.VI) and Piezo Stabilizer window (PiezoStabilizer.VI).

The SubVIs can also communicate with buttons and variables of the main VI or other SubVIs. This is mainly done through Functional Global Variables, which is a design pattern used to control the access to data used in multiple parallel processes [14].

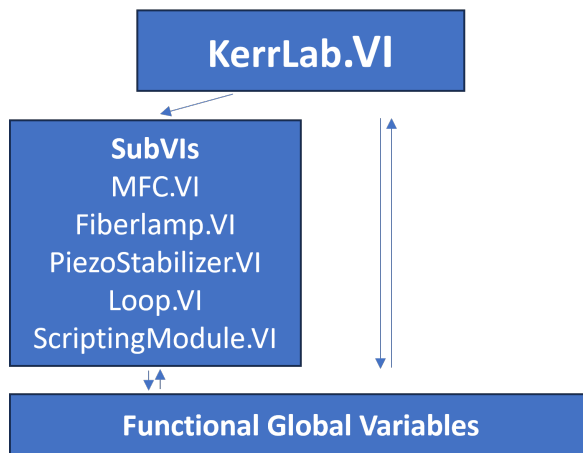


Fig. 4.1: Schematic of the larger components of the KerrLab source code.

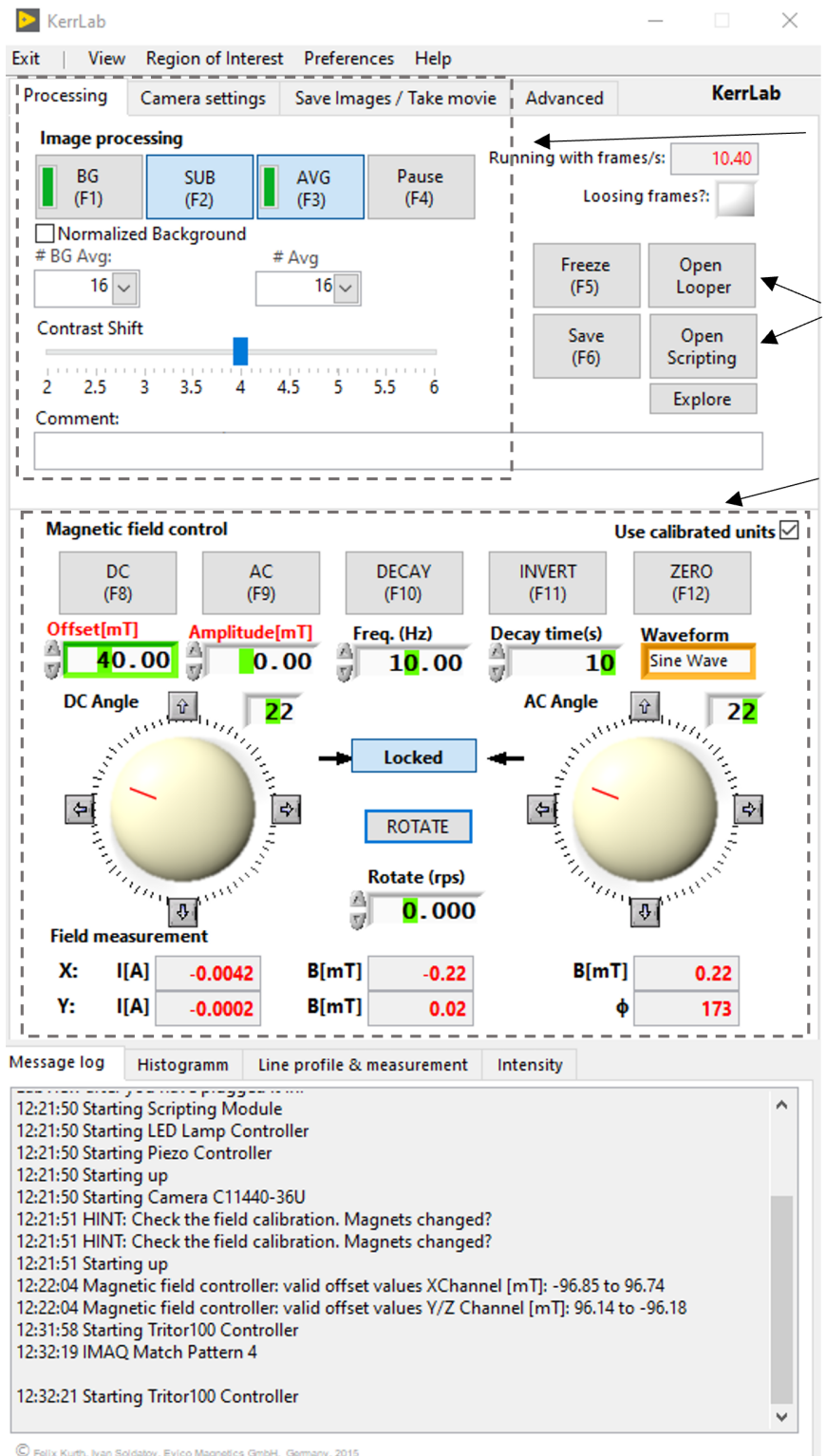


Image
processing
and saving

Access to
FPs of
SubVIs

MFC.VI

Fig. 4.2: The FP of the KerrLab.VI. Contains most of the features used for the MOKE microscope, including image processing, magnetic field control, image and video settings, and access to the FPs of the SubVIs.

4.1.2 Scripting

A prerequisite for achieving automated clocking was the ability to interact with the magnetic field control, and settings for image processing and saving. Attempts to achieve this from an external program on the existing KerrLab executable was proven futile, as much of the functionality needed to access the SubVIs had not been implemented. Additionally, the introduction of an external program would add an extra layer of complexity to the setup, which was deemed unnecessary. Hence, it was decided to implement everything in LabView by expanding the source code, and creating a new KerrLab executable from it.

The plan was to create a separate scripting window where commands could be inputted as text and the program would do the rest. Luckily, an attempt at this by the manufacturer was discovered, containing a working framework for scripting in an existing VI (Scripting-Module.VI). Following this, the VI was imported into the main VI, and a button was added in the main FP to open the scripting window.

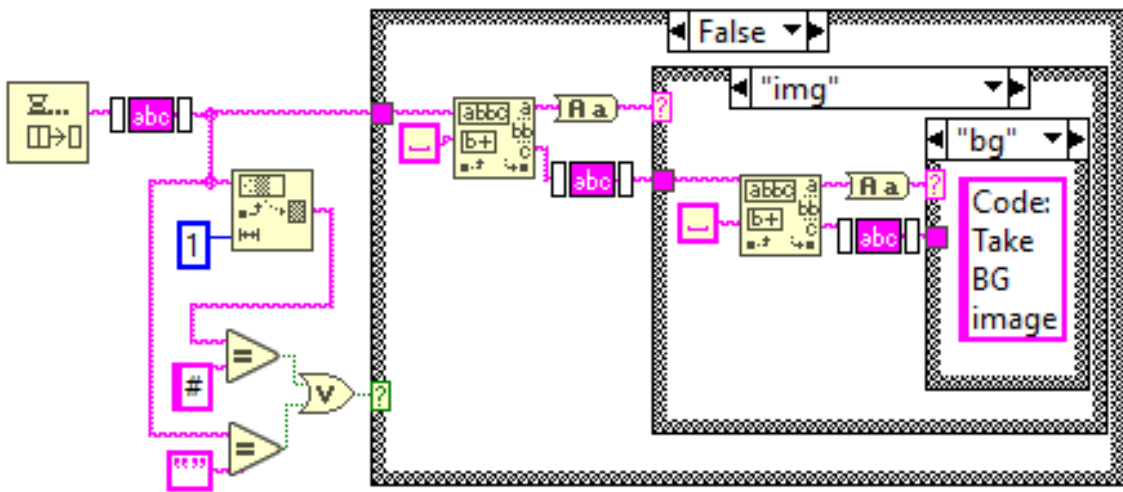


Fig. 4.3: Simplified version of the dequeuing of individual lines from the script. Commands separated by whitespace are used to determine which code is executed.

The scripting is done by placing each line of the text script into a queue, and dequeuing them one by one. A simplified version of the dequeuing is shown in Fig. 4.3. The dequeuer, located to the left, outputs a string, and trailing and leading whitespaces are subsequently removed. The code beneath checks if the string is blank or commented out using a # as first character, which would prevent it from going into the outermost False case. If this is not the case, the string is repeatedly split into two using whitespace as separator, with the leading terms determining which case to execute inwards in the nested case structure.

All case structures require a default, which is executed when the string command is not recognized. The default case is shown in Fig. 4.4. The original framework threw an error as a default, terminating the script. This was changed to instead write a timestamped string with the failed command in the scripting log and turning on an error indicator, seeing that none of the errors posed a critical threat to the program or the experimental setup.

The innermost cases in the nested case structure contains the desired code to be executed, consisting of three vital components. Firstly, the new values that we want to assign to the determined property must be obtained. This can be done by turning the string into a float, which is done if the string is wrapped in <>, as shown in Fig. 4.5. Float and string variables were also implemented using two dictionaries, which can be used to set values to previously defined floats. The float is then rounded to the desired precision.

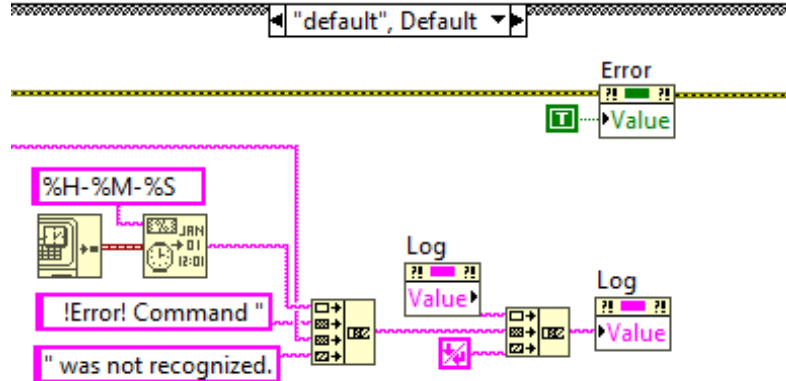


Fig. 4.4: Default case used if the string command is not recognized. Writes an error message in the log and turns the error indicator on.

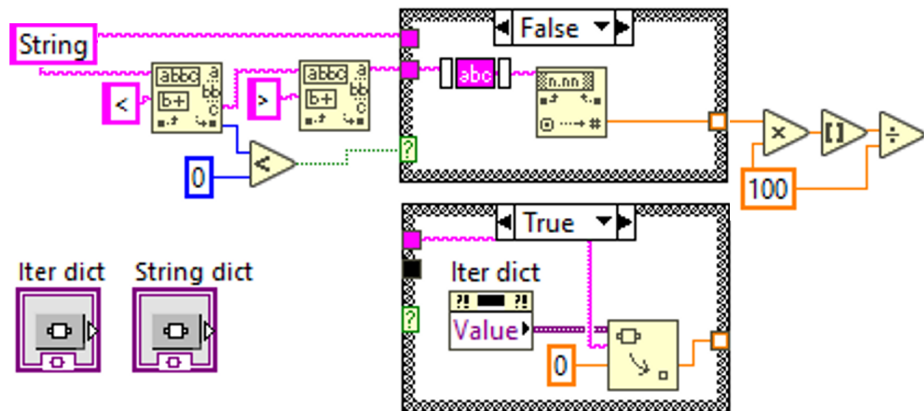


Fig. 4.5: First part of the innermost case structure. Obtains a value from the input string, either by turning the string placed inside <> to a float (False case), or by getting a float from a variable stored in a dictionary, using the string as key (True case). Float is then rounded to the desired precision, being two decimal places in this example.

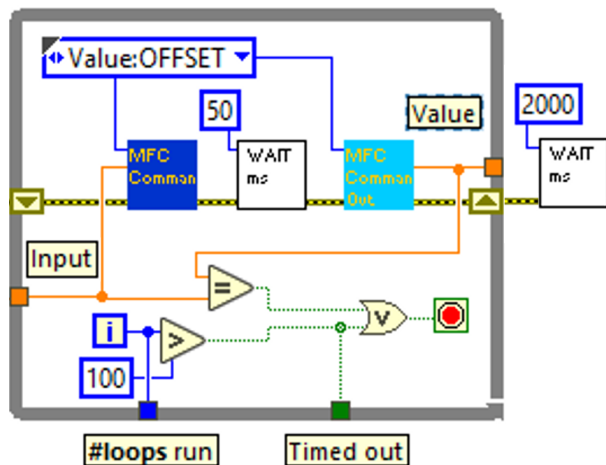


Fig. 4.6: Code for setting a desired property to the acquired input value. Uses a while loop to set the value and read it out again after 50 ms. Loop continues until value has been set correctly or it is timed out. Afterwards, a wait time is added for the voltage controller to stabilize.

Next, the desired property is updated with the obtained input value by writing to a Functional Global Variable. The original framework has been updated with a while loop which sets the value, waits 50 ms, and then reads out the value, as seen in Fig. 4.6. The loop repeats until the value is set correctly, or the loop is timed out as the index i becomes higher than 100. Number of loops run is outputted for statistics. Since it was discovered that the voltage controller powering the electromagnets needed some time to stabilize at the correct value, a wait time was added after the loop. Wait times are tabulated for the different commands in Table 4.1.

Table 4.1: Built-in wait times for different commands.

Command	Wait time (ms)
BG and AVG on	Checks when done, max 5000
AVG off	1500
SUB on/off	1500
DC/AC on/off	2000
Invert	2000
Zero	1500
Offset	2000
Rotate dc/ac*	2000
Image and video	0

*Value was updated to 100 ms after measurements were completed.

Lastly, the log is updated with a timestamped string, including description of the command and the value that has been read out from the Functional Global Variable. If the loop has timed out, a similar message as in the default case is returned, and the error indicator is turned on.

4.2 Testing

The finished script was tested by performing astroid clocking on two 45° pinwheel ASIs of different sizes, 50×50 (5100 magnets) and 100×100 (20200 magnets), indexed as structures 11.8 and 12.8 respectively. A schematic of the lithography mask is shown in Fig. 4.7.

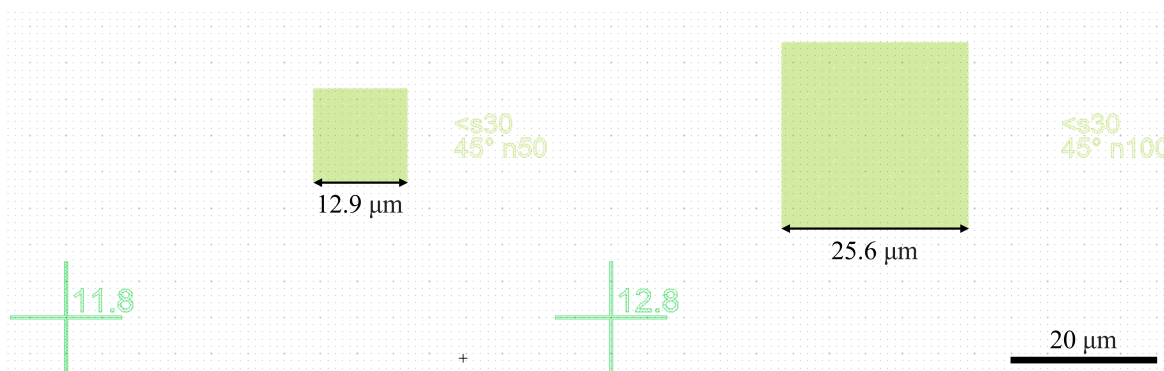


Fig. 4.7: Lithography mask of the two 45° pinwheel ASI structures investigated, with index 11.8 denoting a 50×50 (5100 magnets) structure and 12.8 denoting a 100×100 (20200 magnets) structure.

The ASIs were initially polarized using 72 mT applied along 0° and 180° to obtain an image of the positive and negative saturation magnetization respectively. With the ASIs polarized along 180°, a background image was taken before the clocking commenced. Automatic AB-clocking was performed for 35 cycles to grow domains using the previously described angles, before ab-clocking was performed for 15 cycles. Images were taken after each of the 50 cycles, with clocking index and type annotated automatically in the images.

The images were taken with magnetic contrast in the pure transverse direction, using strobing of LEDs 5 and 6 followed by 7 and 8 and subtracting the images. Each image captured was the average of 16 frames, which was done to remove noise. These images were in turn subtracted from the acquired background image to image the change in magnetization during clocking.

4.3 Image processing and plotting

The images were used to make time series to visualize the growth of domains within the ASIs, and plots of the magnetization of the ASI as a function of the discrete clocking steps. The raw ASI pixel values were gathered from the part of the images containing the ASI using a mask, as visualized in Fig. 4.8. The plan was to use the two images of the saturated magnetization to transform raw pixel values into magnetization values.

The initial attempts revealed a significant drift in overall brightness within all image sequences. To correct for this, an area of 100×100 pixels outside the ASI was chosen to serve as a reference. Since no change in magnetization was expected outside the ASI, the change in mean pixel value inside the reference box was subtracted from the raw ASI and raw saturation magnetization pixel values.

The mean of the corrected ASI pixel values were subsequently transformed to create a plot of the magnetization, using the positive and negative saturation magnetization as calibration. For the time series, the saturation magnetization values were not used. Instead, the contrast was optimized for the images of the corrected ASI pixel values by setting the lowest and highest pixel value of the whole sequence as the minimum and maximum color values.

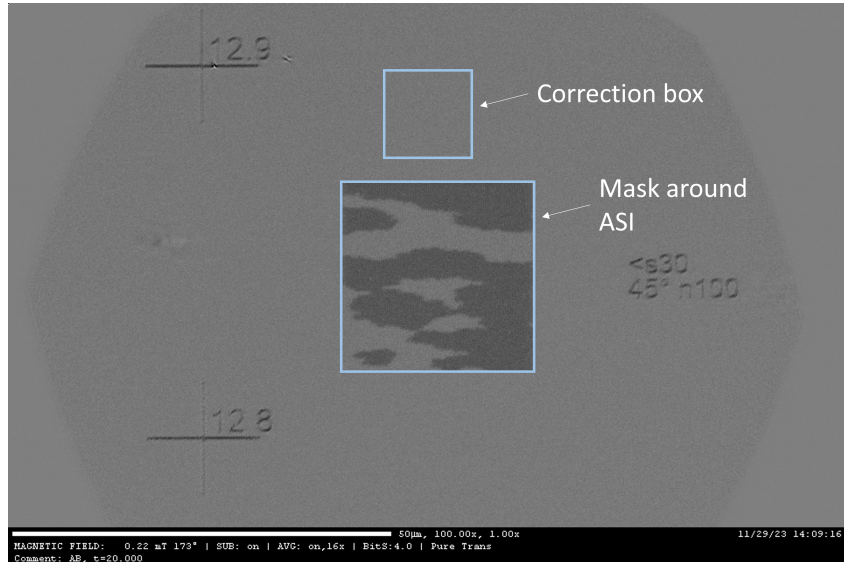


Fig. 4.8: Visualization of the mask used to obtain ASI values and the correction box placed on a raw image.

Chapter 5

Results and discussion

5.1 Scripting FP

An annotated image of the finished scripting FP is shown in Fig. 5.1. Label 1 shows the text box used for script commands. The script used for astroid clocking is attached in Appendix A.1, utilizing variables and for loops. A complete list of the implemented commands is labeled as 2, and is attached in Appendix A.2. Label 3 shows the timestamped log, which can be saved to a .txt file. Buttons to run or stop the script, as well as checking whether the commands are valid or not are labeled as 4. Development versions of these four features were included in the original framework, but have been greatly modified.

Label 5 indicates a global variable that is incremented by one after the script finishes, which was implemented to easily update image paths with run index for subsequent runs. The possibility to import and export scripts as .txt is labeled as 6. Label 7 shows the error indicator, which is turned on if a non-critical scripting error occurs. Label 8 shows the two dictionaries used for variables. These four features are all new.

5.2 Image processing

Results for the image processing is presented for a clocking sequence on structure 11.8 using a field strength of 33 mT, referenced later as Run 0. A time series of the evolution of the system is shown in Fig. 5.2, with bright areas corresponding to magnets with a negative component along the x-axis and dark areas corresponding to positive. The processing worked well to achieve an even brightness over the whole stack. An attempt to increase the contrast of the images using the minimum and maximum pixel value in each individual image as minimum and maximum color value is shown in Fig. A.1. This proved unsuccessful, due to a large variation in the extreme point pixel values from one image to the next.

The mean of the raw ASI pixel values, the positive and negative saturation magnetization pixel values and the reference box pixel values are plotted in Fig. 5.3a. A clear drift in brightness is observed, as even though inspection of the first and last image show that they are clearly the same state, there is a significant difference in the mean pixel value. The drift of the correction and the raw ASI values seems to be closely correlated.

Fig. 5.3b shows the ASI pixel values and saturation magnetization values after being corrected for the drift in image brightness, which was done by subtracting the difference in the correction values for each time step compared to the first image. The mean pixel values are approximately the same at $t=0$ and $t=50$, which coincides well with expectations from inspection of the time series. Additionally, all values seems to be contained between the indicated saturation values.

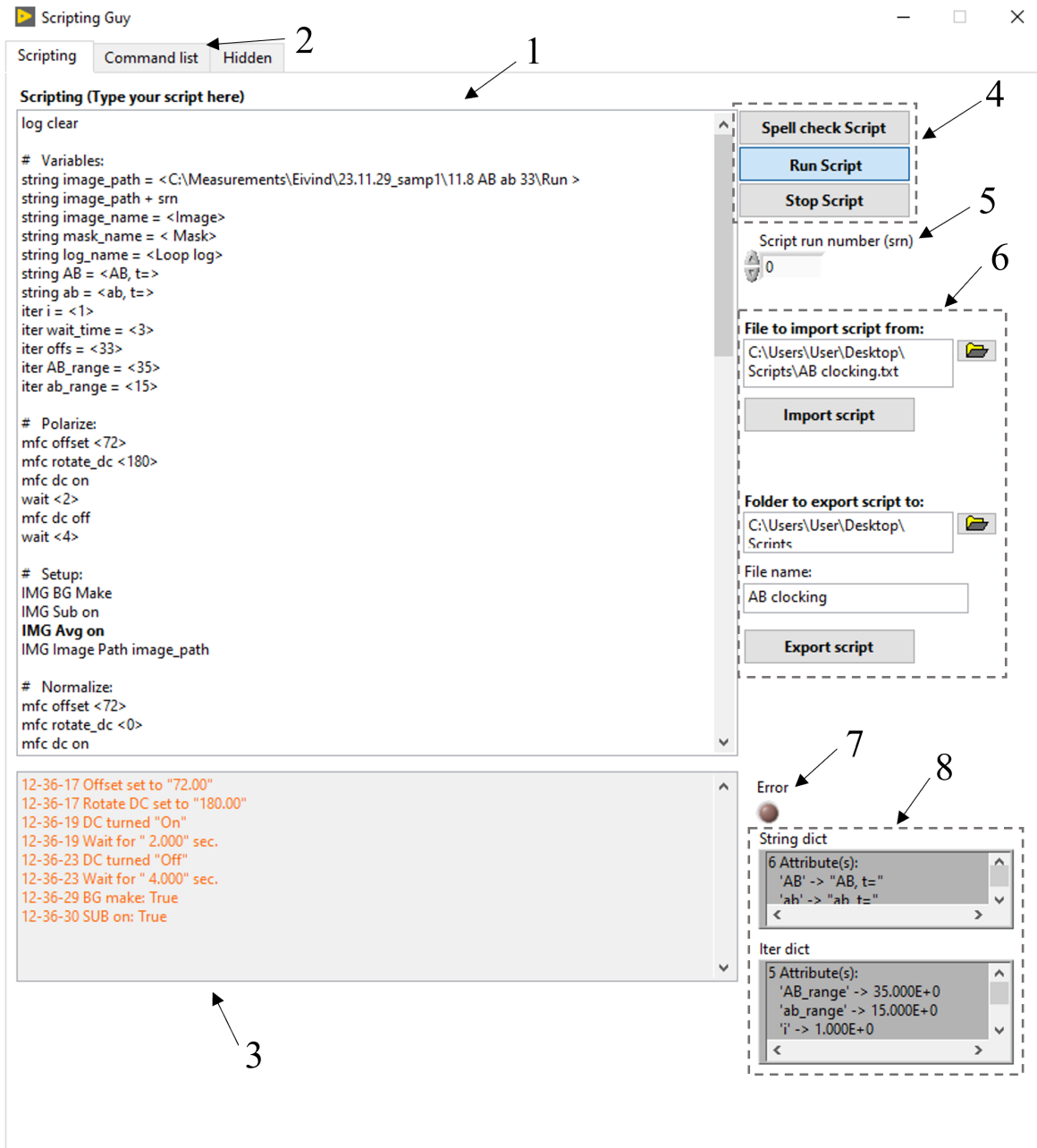


Fig. 5.1: Annotated image of the finished scripting FP. 1. Text box for script commands. 2. List of all implemented commands. 3. Timestamped log. 4. Buttons to run and stop the script, as well as a button to check whether all the commands are valid or not. 5. Global variable that is incremented by one when the script finishes. 6. Options to import and export scripts as .txt. 7. Error indicator. 8. The two dictionaries used for string and float variables.

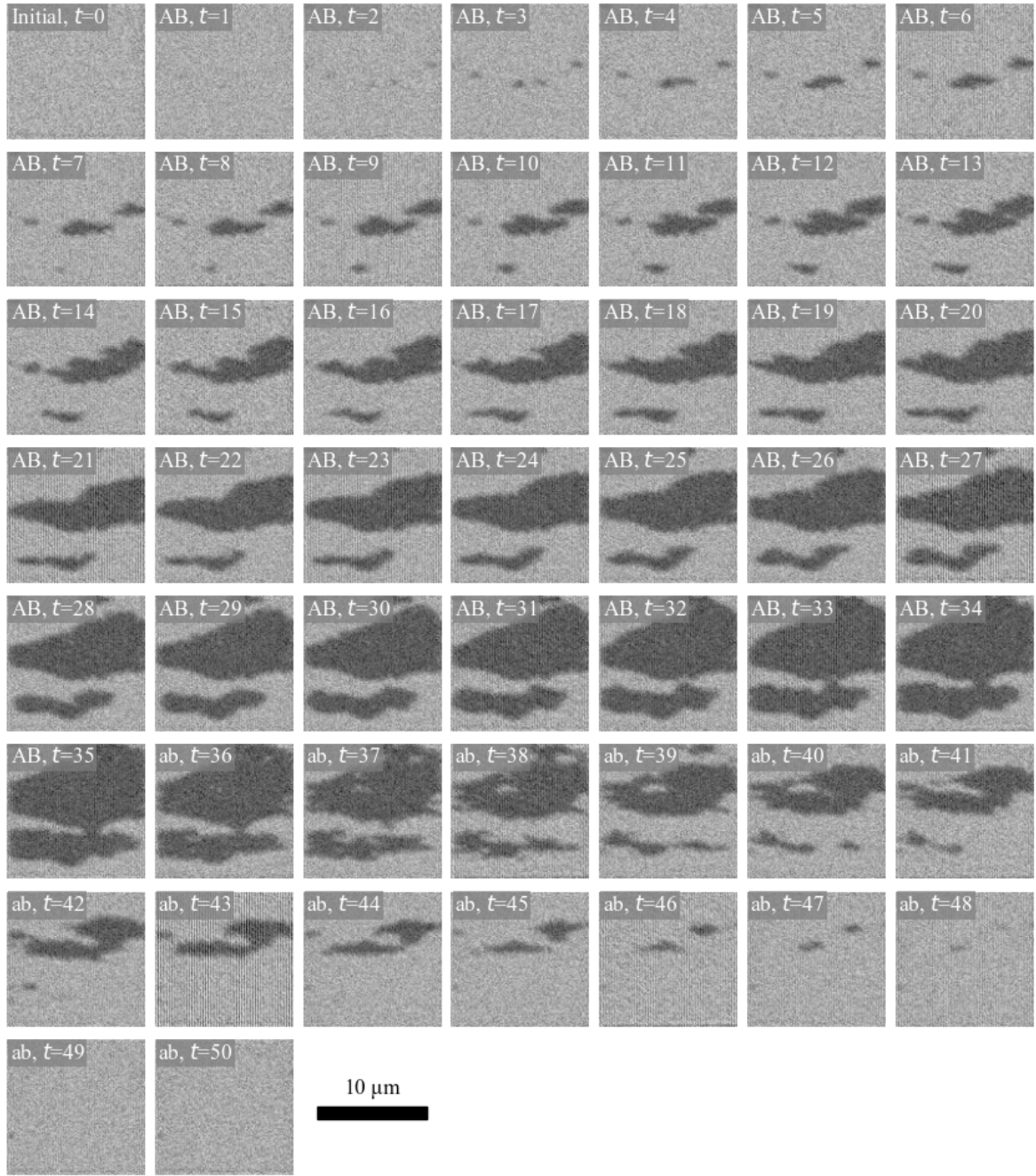


Fig. 5.2: Time series of Run 0 of a clocking sequence on structure 11.8 using a field strength of 33 mT. Shows 35 cycles of AB-clocking, followed by 15 cycles of ab-clocking.

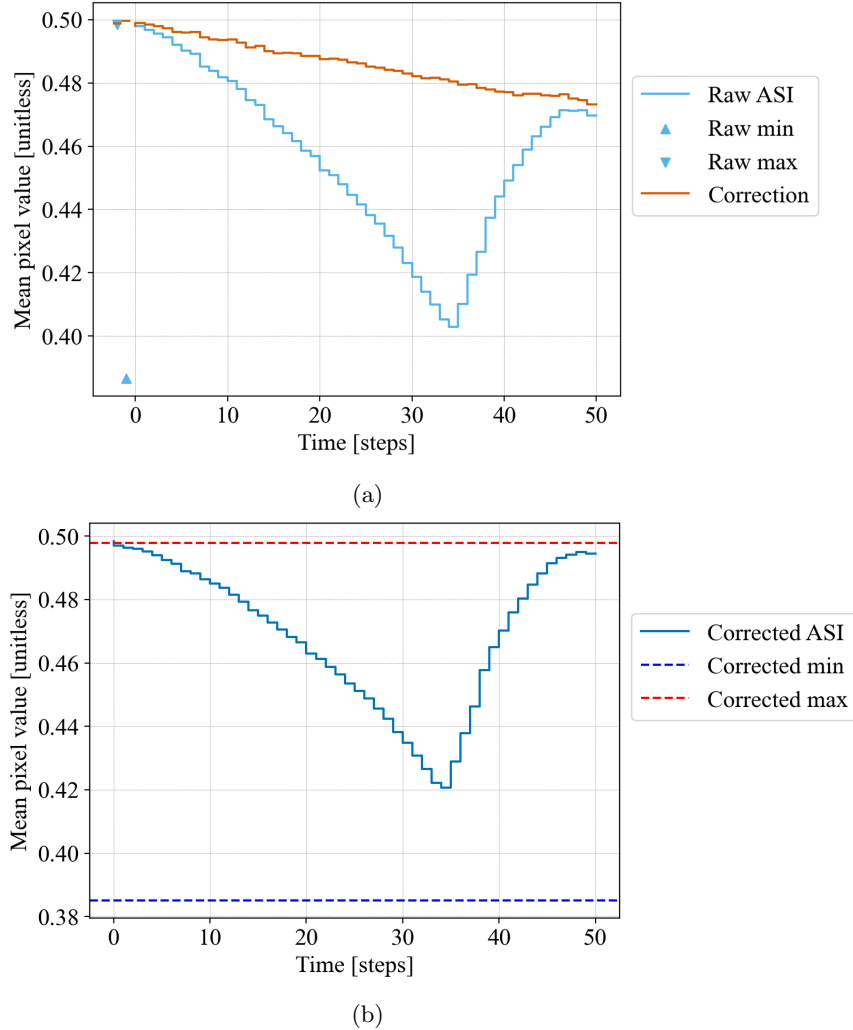


Fig. 5.3: Mean pixel values plotted for (a) the raw ASI, positive and negative saturation magnetization and correction. A clear drift in brightness is observed. (b) the ASI and saturation magnetization after being corrected for the drift in brightness. All values seems to be contained between the saturation values, and fits better with what is observed in the time series.

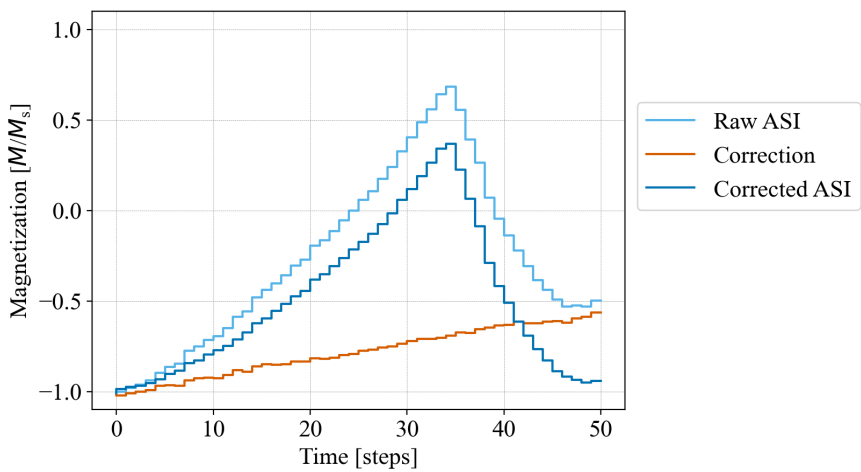


Fig. 5.4: Plot of magnetization from the transformed pixel values. Positive magnetization is chosen along positive x-axis. At first glance, the correction seems to address the drift issue sufficiently well.

Magnetization is plotted in Fig. 5.4 from the transformed pixel values in the previous figures, using the positive and negative saturation magnetization pixel values for calibration. Positive magnetization was chosen along the positive x-axis, to more easily compare with results from the paper by Jensen and Strømberg et al. [6]. The image processing seemed to work well for the corrected ASI values, and was therefore used for the rest of the results.

5.3 Automated astroid clocking

5.3.1 Hysteresis

Hysteresis measurements were performed on the 11.8 structure to obtain H_c , serving as an upper limit for the possible field strengths available for use in astroid clocking. Measurements taken along 0° and 22° are plotted in Fig. 5.5, measured from -60 mT to 60 mT and back again. Field steps were chosen as 0.5 mT around the expected value for H_c and set to 4 mT elsewhere.

Zero magnetization was observed at 33.3 mT and -33.7 mT for 0° , and at 36.8 mT and -36.7 mT for 22° . The difference in the positive and negative value could be explained by an additional drift in the brightness of the images that has not been resolved by the correction. This is reflected by the magnetization not reaching the saturation in the last value of the plot, despite images indicating that it has saturated. Hence, H_c was set to the positive measured value.

The difference in H_c for the two angles could be explained by the astroid plot in Fig. 2.5a. For 0° , magnets in both sublattices L_a and L_b flip at the same field strength, which may explain why flipping of large domains are observed in Fig. 5.6a. For 22° , we expect magnets in L_a to flip at a lower field strength than at 0° and magnets in L_b at a higher, causing the hysteresis curve to switch in two steps, as discussed in a paper by Li et al. [15].

The fact that we don't observe this in our measurements, seems to indicate that the two magnet sublattices are tightly linked, and that the switching of magnets in sublattice L_a at lower fields is impeded by the lack of switching in L_b , increasing H_c . This might also explain the more fractured growth seen in Fig. 5.6b, as switching occurs at different fields depending on how connected the magnets are within the different regions.

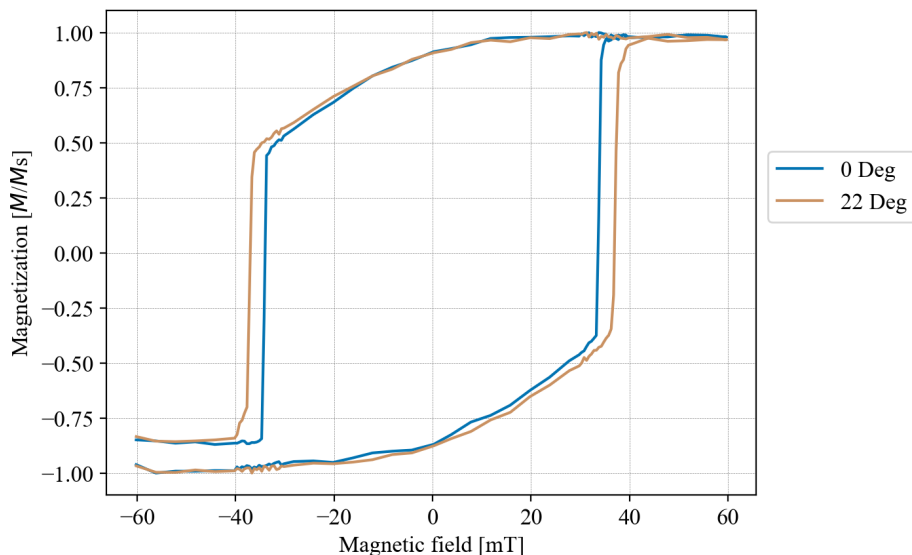


Fig. 5.5: Hysteresis plot performed on the 11.8 ASI structure at 0° and 22° .

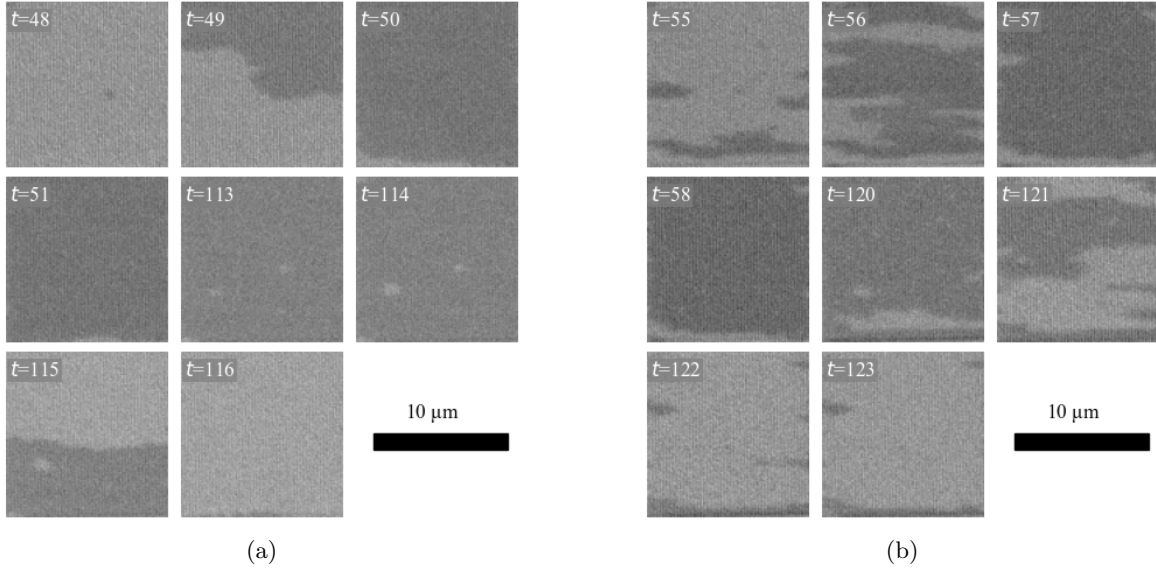


Fig. 5.6: Images from hysteresis measurements around H_c for (a) 0° . (b) 22° .

5.3.2 Clocking at 30 mT, 32 mT and 33 mT

The clocking sequence was performed at three different field strengths below H_c , namely 30 mT, 32 mT and 33 mT. A subset of the resulting images is shown in Fig. 5.7. No visible growth was observed for 30 mT, some growth for 32 mT, and a significant growth for 33 mT. Hence, 33 mT was used in the subsequent measurements.

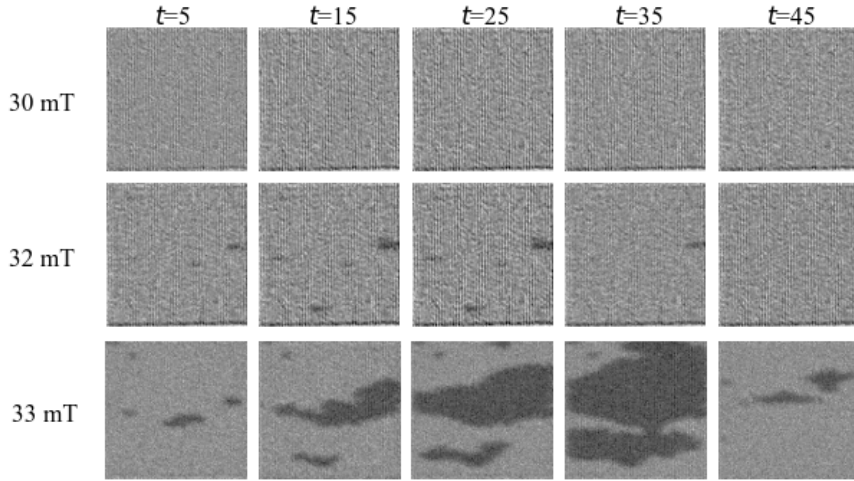


Fig. 5.7: Comparison of domain growth at time t from clocking on structure 11.8 using three different field strengths. Large differences in growth rate are observed.

5.3.3 Comparison of manual, automated and reference clocking

A clocking sequence was performed manually on the 11.8 structure with 33 mT to compare with the automated clocking. The time series for the manual clocking is attached in Fig. A.2. The results are plotted in Fig. 5.8, with results from the paper by Jensen and Strømberg et al. [6] serving as a reference.

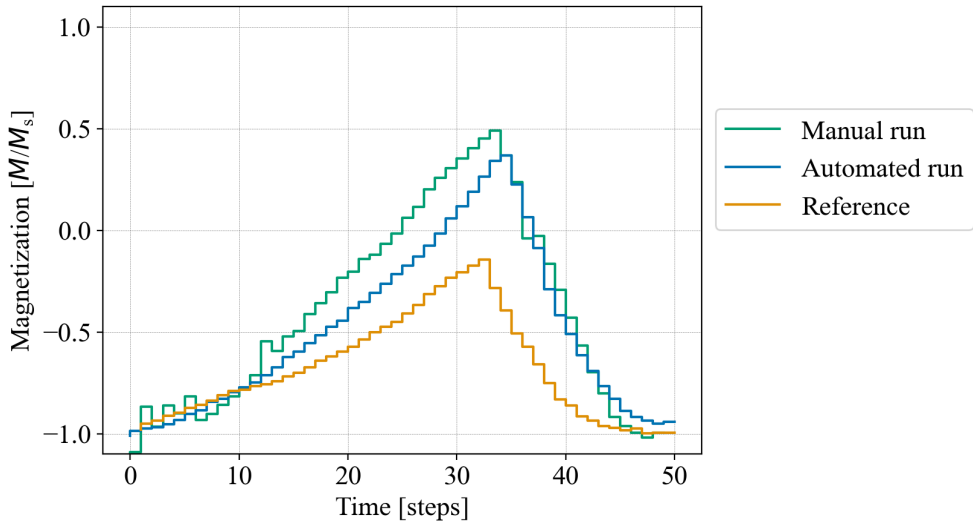


Fig. 5.8: Magnetization plot of the 11.8 structure for manual and automated clocking, using results from the paper by Jensen and Strømberg et al. [6] as reference. The main property of interest is the overall shape of the plot, as the reference uses a different sample and field strength.

The manual clocking was found to be the most irregular of the plots, especially for the first few cycles. This is presumably caused by a too small wait time between the field was turned off and image being taken. This was noticed after a few cycles, and the subsequent cycles seem more consistent. However, this highlights one of the advantages with automated clocking. The clocking took 20 minutes in total, and the timestamps indicate that an image was acquired for every clock cycle, although ab-clocking was begun one cycle too early. Images of saturation magnetization was taken after the clocking, which explains why the drift that has not been accounted for is observed at $t=0$ and not $t=50$.

The automated clocking seems to be very consistent, with no observed peaks or irregularities. Both the manual and automated clocking seems to replicate the overall shape of the reference plot successfully. As the reference uses a different sample and field strength, it is the general shape of the curve which is of interest. The shape is recognized by a slow growth in the beginning as domains start to form, and more rapid growth after some cycles as the domain growth is catalyzed along the formed domain borders. A more rapid reversal than initial growth is also observed in all plots. This strengthens the notion that the automation works as intended.

5.3.4 Unidirectional clocking

To confirm that the alternating clocking of A and B is what drives domain growth, ten cycles of A-clocking and B-clocking were performed before and after ten cycles of AB-clocking. The resulting plot is shown in Fig. 5.9. The plot substantiates the presented theory well, as no growth is observed within any of the cycles with constant angle. A large growth is observed in the ten cycles of AB-clocking as expected. Growth equaling one AB-cycle is also observed in the transitions between A-clocking and B-clocking, being largest for the later steps as more domain borders have been formed.

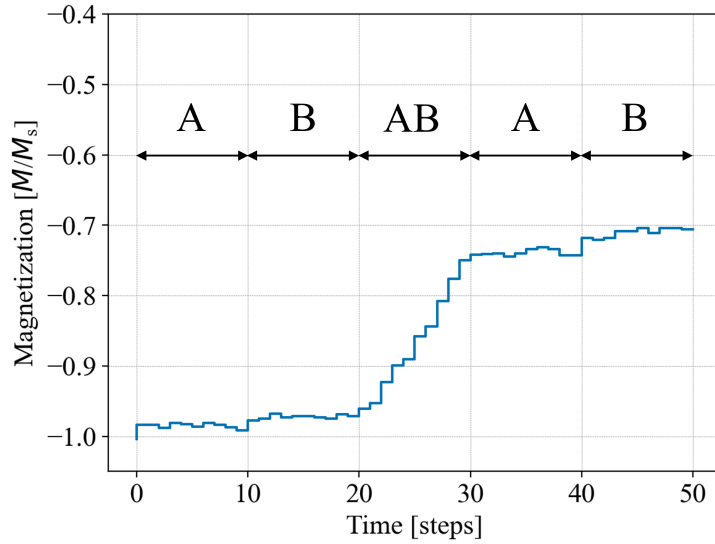


Fig. 5.9: Ten cycles of A-clocking and B-clocking were performed before and after ten cycles of AB-clocking. Growth was only observed during AB-clocking, as well as the transitions between A-clocking and B-clocking, matching our expectations.

5.3.5 Multiple automated runs

Ten clocking sequences were performed in quick succession on the 11.8 structure with 33 mT to obtain statistical data of how the automation performs over time, but also to investigate the reproducibility of the results. A scatter plot of the ten sequences is shown in Fig. 5.10a, while the mean and standard deviation of the same data is shown in Fig. 5.10b. The data shows that the magnetization of the ASI at each time step is very similar between runs, which is promising for the utilization of ASIs for computation.

A subset of the images for all the runs, as well as the mean of each pixel value for the given time step, is shown in Fig. 5.11. The images also show that the runs are very comparable, not only in the total magnetization of the ASI, but also in the spacial distribution of the grown domains. Growth is initialized in the same few distinct positions every time. The distribution of these positions seem random, but are believed to be caused by small defects in these locations reducing the required switching field. The results indicates that adding patterned defects might work well to control where growth is initiated in the future.

Each clocking sequence took 14 minutes and 12 seconds to complete. However, this could easily be optimized further if desired. The reduction of rotation wait time from 2000 ms to 100 ms, which was done after the measurements were completed, would have decreased the sequence time by 3 min and 16 sec for each run. This constitutes a major improvement compared to the manual clocking, both in terms of sequence time, human resources, consistency and reproducibility of the clocking.

The temperature was monitored during the repeated clocking sequences, in case the continuous clocking would cause the electromagnets to heat up. No significant increase in temperature was reported for the relatively small magnetic fields applied for this work.

During the ten runs, 1030 rotations of the field angle were performed in total. For 93 of these, the rotation angle was not set correctly on the first attempt. However, they were all corrected by the while loop described in Fig. 4.6. These errors constitute 9.0% of the performed rotations, and underlines the significance of the error loop implementation. The underlying source of the error remains unexplained.

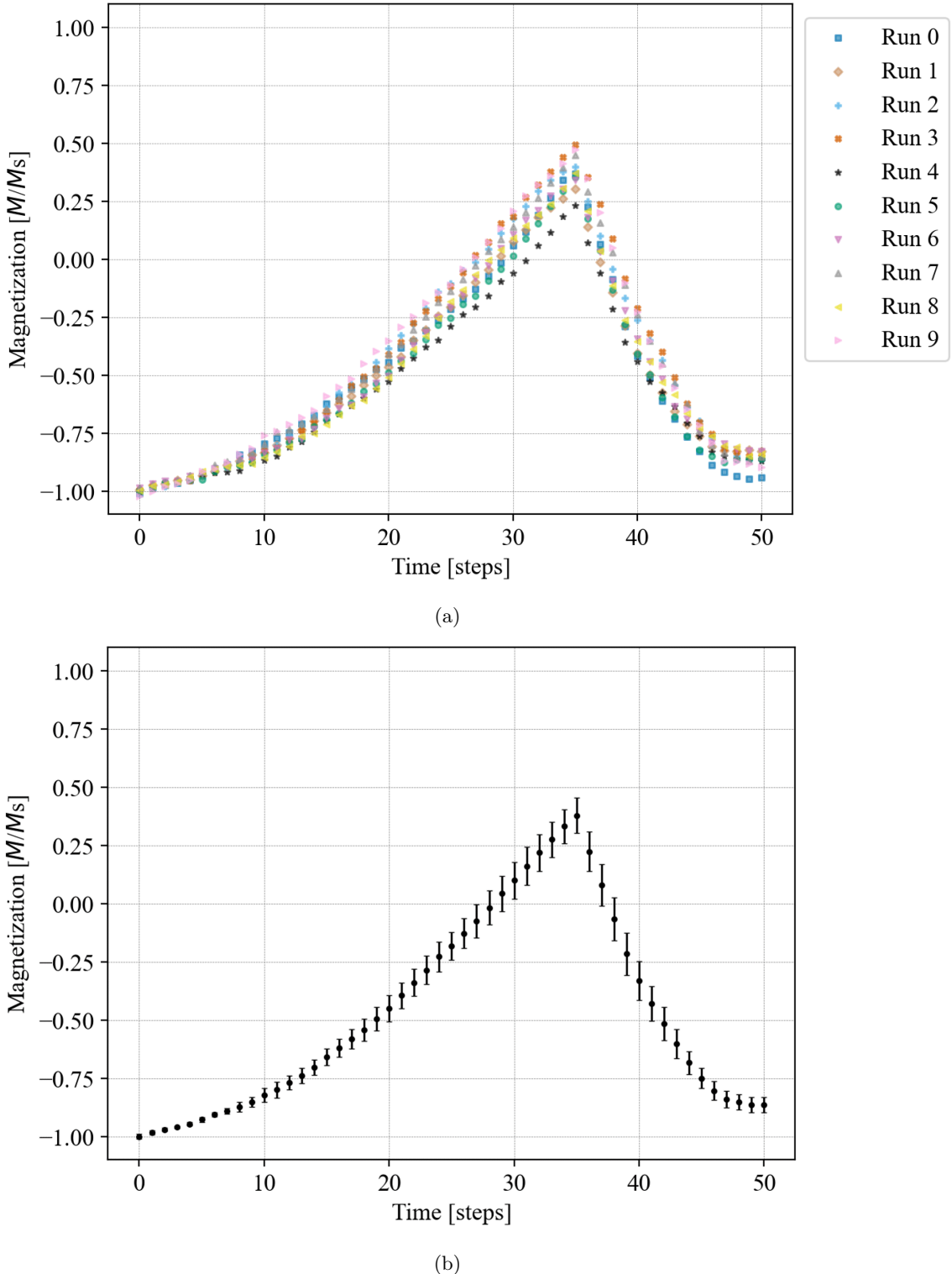


Fig. 5.10: Plots for the ten runs performed on the 11.8 structure using field strength of 33 mT as (a) scatter plot and (b) mean values with standard deviation. The runs are very comparable, indicating that the clocking sequences produce reliable structures with a high degree of reproducibility. This is also reflected in the small standard deviations.

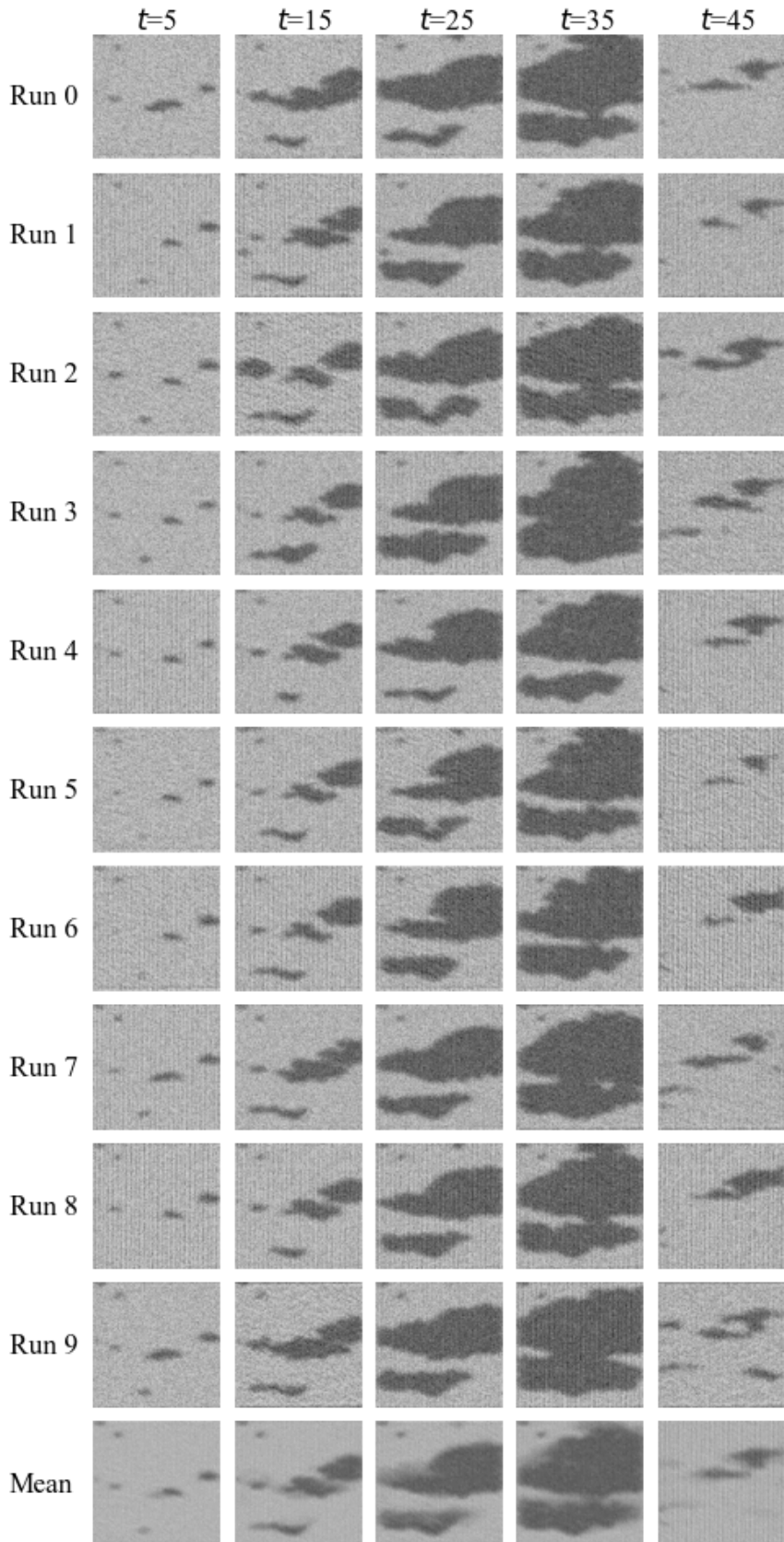


Fig. 5.11: A subset of the images for the ten runs at specified times t , as well as the mean of each pixel value for the given time step. Shows that both the magnetization and where domain growth is facilitated is very predictable for all runs. Growth being initialized at seemingly random points in the ASI is believed to be caused by small defects, reducing the required switching field.

5.3.6 Validation of image processing

To check the validity of the correction and transformation performed for the plotting of the magnetization of the ASI, the clocking sequence was performed on the 12.8 structure using a field strength of 32 mT. The clocking field was sufficiently strong to flip more or less all the magnets during the AB-clocking, providing a new reference value for the saturation magnetization to compare with the calibration values. The resulting plot is shown in Fig. 5.12. The result strengthens the hypothesis that there is an additional drift in brightness which has not been accounted for, as the plot has a maximum of 1.1 and doesn't return to -1.0 after 50 cycles. The last effect is also seen in the plots for the multiple automated runs.

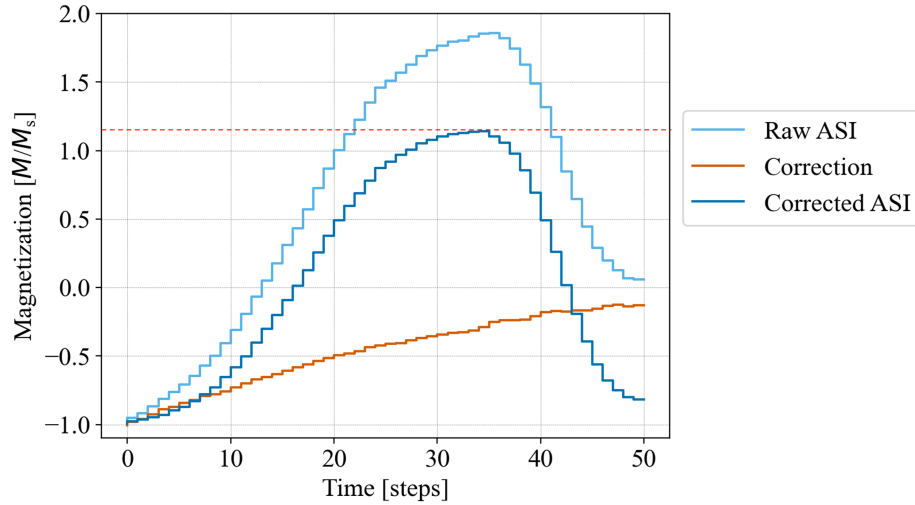


Fig. 5.12: Control measurement performed on the 12.8 structure using 32 mT. Clocking field was sufficiently strong to saturate the magnetization during the AB-clocking, providing a new saturation magnetization to compare with the calibration.

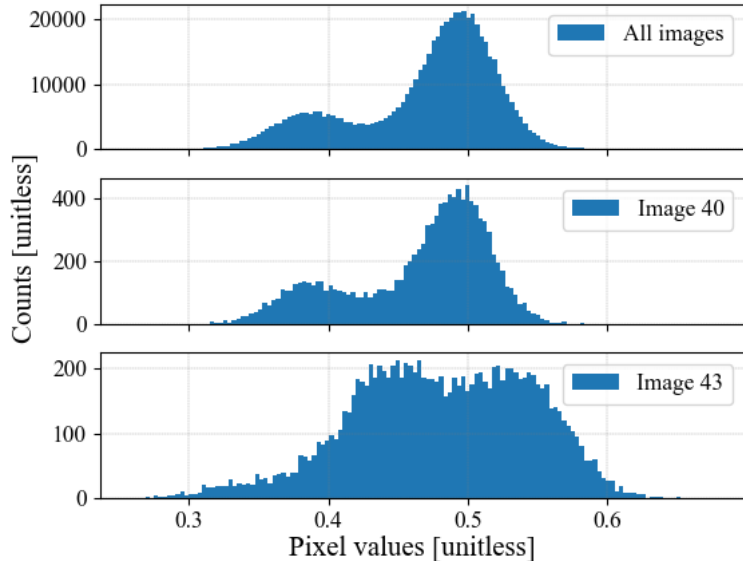


Fig. 5.13: Histogram of the pixel values of all the images, image 40 and image 43. The highest peak correspond to light values and the lower to dark. Image 43 deviates strongly from the shape of the other two, which is caused by noise in the acquired image.

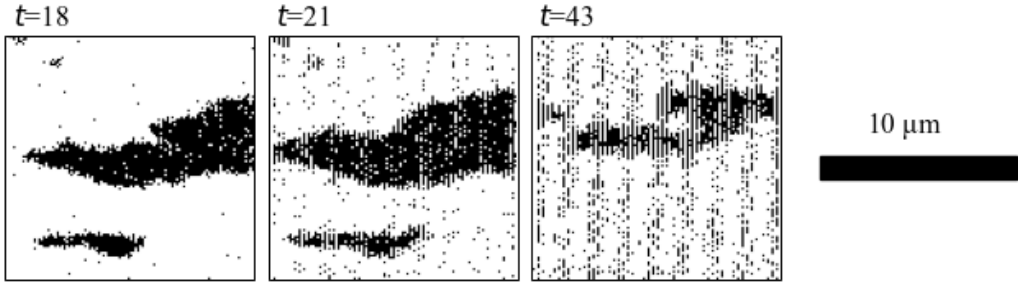


Fig. 5.14: Three images of the processed data using threshold. Works well from most of the images, but also enhances noise as seen for $t=43$.

An attempt to solve this issue was explored using thresholds. The idea was to map the pixel values into either -1 or 1, ensuring that the mean magnetization remains between these values and removing the need for images of saturation magnetization in the beginning.

A histogram of all the pixel values corrected for drift for the 11.8 structure during the run 0 for 33 mT is shown in Fig. 5.13. The histogram contains two peaks, with the highest peak corresponding to the light values and the lower to the dark. Histograms for individual images seem to closely resemble the histogram for all pixel values, as visualized with image 40, which seemed promising for the implementation. However, some images greatly deviate from this histogram, exemplified by image 43. In these cases, thresholding will probably not work optimally.

The irregularities of the peaks in some of the histograms are caused by vertical noise in the raw images, as seen in the time series in Fig. 5.2 for $t=43$. This is believed to occur due to a small shift in the focus in the live image compared to the subtracted background image. When the contrast of the two domain types are enhanced using a threshold, this noise is also enhanced, as shown in the thresholded images in Fig. 5.14.

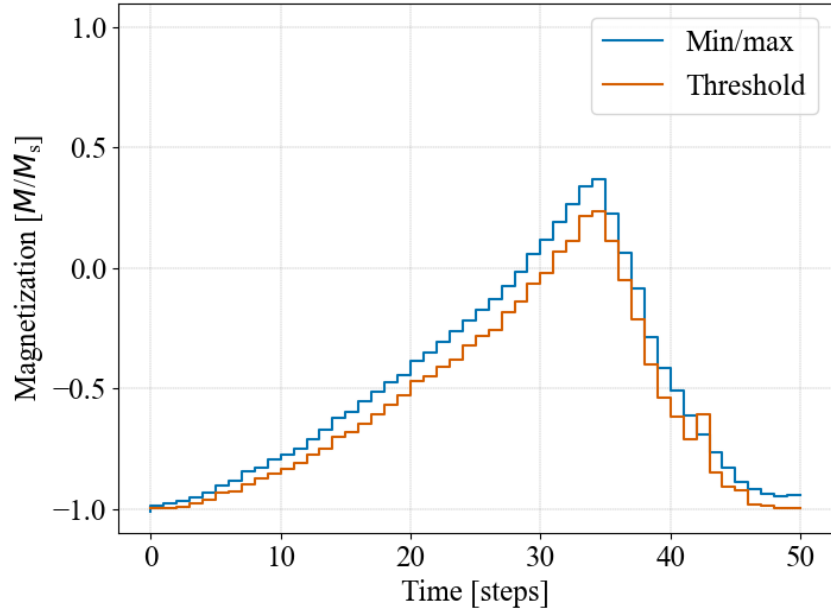


Fig. 5.15: Plot of magnetization comparing old and new image processing. The method using a threshold solves the issues with saturation magnetization by design, but seems to enhance noise in the data as seen for $t=43$.

CHAPTER 5. RESULTS AND DISCUSSION

From inspection of the topmost histogram in Fig. 5.13, the value of 0.427 was chosen as threshold value. A plot comparing the magnetization using the old and new image processing is shown in Fig. 5.15. The new method solves the drift issue by design, and seems reasonable upon first inspection compared to the other plots and images. The only irregularity observed is a sharp peak for image 43, as expected from its histogram and thresholded image.

The new method seems promising, but more investigation is needed for correction of noise and automation of how threshold values is selected. An evaluation of whether useful information is lost after using the threshold should also be considered, depending on the desired application.

Chapter 6

Conclusion and outlook

In this thesis, an automation of the functionality of a MOKE microscope using scripting was developed and tested using astroid clocking. The implementation seems to work well, with few observed errors or bugs. The observed error for the rotation of the magnetic field during the development stage seems to have been resolved by the addition of the error loop. The implemented scripting commands, such as for the magnetic field control, image capturing, for loops and variables, seems to cover a wide range of applications and uses. The scripting constitutes a huge improvement compared to manual handling, both in use of human resources, run time, and reproducibility and uniformity of the results.

The measurements done with automated astroid clocking substantiates the presented theory well. Alternated A- and B-clocking has been shown to be the driver behind domain growth, as little to no growth is observed for the unidirectional clocking. The time evolution of both the total magnetization and the spacial distribution of the grown domains is largely similar for the multiple repeated runs, strengthening the notion that the scripting works as intended, as well as being promising for the use of ASIs for unconventional computing. Growth is seen to initiate in the same few, seemingly random, regions of the sample, suspected to be caused by small defects. This indicates that the use of fabricated defects might be a good method to control where growth is initiated in the future.

Corrections for the observed drift in brightness over the image stack using a reference box seem to work quite well, but is still unable to remove all of the drift. This resulted in the magnetization plots not being contained by the defined saturation magnetization. An attempt to solve the issue using thresholding is explored, solving the previous issue by design. The new method seems promising, but more exploration into the removal of noise from the image data is required.

The successful automation opens up for a lot of possibilities for future work and exploration. Trying to implement more complex clocking procedures and obtaining more control over the growth of the domains, including where growth is initialized, seem like a reasonable step forwards.

With regards to the script and the setup, the implementation easily allows for more functionality to be implemented if needed. The focus during the development has mainly been towards functionality and getting things to work, while less effort has gone into the optimization of every process. This is exemplified by the built-in wait times, which should be improved further. For the current setup, the sample stage is moved manually, which restricts the automated clocking sequences to one structure. The ability to move the sample between structures automatically would be a logical next step for the automation.

Bibliography

- [1] Aimee Ross and Lorna Christie. Energy consumption of ICT. <https://post.parliament.uk/research-briefings/post-pn-0677/>. Accessed: 2023-12-11.
- [2] Arthur L. Robinson. Problems with Ultraminiaturized Transistors. *Science*, 208(4449):1246–1249, 1980.
- [3] John Michael David Coey. *Magnetism and Magnetic Materials*. Cambridge University Press, 2010.
- [4] R. Wang, C. Nisoli, and R. et al. Freitas. Artificial ‘spin ice’ in a geometrically frustrated lattice of nanoscale ferromagnetic islands. *Nature*, 439:303–306, 01 2006.
- [5] Sandra Skjærvø, Christopher Marrows, Robert Stamps, and Laura Heyderman. Advances in artificial spin ice. *Nature Reviews Physics*, 2, 11 2019.
- [6] Johannes Jensen, Anders Strømberg, Ida Breivik, Arthur Penty, Michael Foerster, Miguel Niño, Muhammad Khalil, Gunnar Tufte, and Erik Folven. Clocked dynamics in artificial spin ice. 06 2023.
- [7] Nicola A. Spaldin. *Magnetic Materials: Fundamentals and Applications*. Cambridge University Press, 2 edition, 2010.
- [8] Mathias Getzlaff. *Fundamentals of Magnetism*. Springer Berlin, Heidelberg, 2007.
- [9] N. S. Bingham, S. Rooke, J. Park, A. Simon, W. Zhu, X. Zhang, J. Batley, J. D. Watts, C. Leighton, K. A. Dahmen, and P. Schiffer. Experimental realization of the 1d random field ising model. *Phys. Rev. Lett.*, 127:207203, Nov 2021.
- [10] C. Tannous and J. Gieraltowski. The stoner–wohlforth model of ferromagnetism. *European Journal of Physics*, 29(3):475, mar 2008.
- [11] Jeffrey McCord. Progress in magnetic domain observation by advanced magneto-optical microscopy. *Journal of Physics D: Applied Physics*, 48(33):333001, jul 2015.
- [12] I. V. Soldatov and R. Schäfer. Selective sensitivity in Kerr microscopy. *Review of Scientific Instruments*, 88(7), 07 2017.
- [13] National Instruments. LabView. <https://www.ni.com/en-no/shop/product/labview.html>. Accessed: 2023-11-07.
- [14] Ed Doering. Rio developer essentials guide for academia, 2018.
- [15] Y. Li, G. W. Paterson, G. M. Macauley, F. S. Nascimento, C. Ferguson, S. A. Morley, M. C. Rosamond, E. H. Linfield, D. A. MacLaren, R. Macêdo, C. H. Marrows, S. McVittie, and R. L. Stamps. Superferromagnetism and domain-wall topologies in artificial “pinwheel” spin ice. *ACS Nano*, 13(2):2213–2222, 2019. PMID: 30588800.

Appendix A

Scripting

A.1 AB ab script

```
# Beginning of script
log clear
# Variables:
string image_path = <C:/Measurements/Eivind/23.11.29_samp1/11.8 AB ab 33/Run >
string image_path + srn
iter i = <1>
iter offs = <33>
iter AB_range = <35>
iter ab_range = <15>

# Polarize:
mfc offset <72>
mfc rotate_dc <180>
mfc dc on
wait <2>
mfc dc off
wait <4>

# Setup:
IMG BG Make
IMG Sub on
IMG Avg on
IMG Image Path image_path

# Image negative and positive saturation magnetization:
mfc offset <72>
mfc rotate_dc <0>
mfc dc on
wait <2>
mfc dc off
wait <4>
IMG Image Name <Image Min>
IMG comment <Min>
Img image save
```

APPENDIX A. SCRIPTING

```
mfc rotate_dc <180>
mfc dc on
wait <2>
mfc dc off
wait <4>
IMG Image Name <Image Max>
IMG comment <Max>
Img image save

# Clocking
mfc offset offs
IMG Image Name <Image>
IMG comment <Initial, t=0>
Img image save

for <13>; AB_range
string comment = <AB, t=>
string i str i
string comment + i
IMG comment comment
mfc Rotate_DC <22>
mfc dc on
mfc dc off
mfc Rotate_DC <338>
mfc dc on
mfc dc off
wait <3>
IMG Image Save
iter i + <1>

for <13>; ab_range
string comment = <ab, t=>
string i str i
string comment + i
IMG comment comment
mfc Rotate_DC <202>
mfc dc on
mfc dc off
mfc Rotate_DC <158>
mfc dc on
mfc dc off
wait <3>
IMG Image Save
iter i + <1>

img sub off
img avg off
log save image_path; <Loop log>
# End of script
```

A.2 Script commands

used for comment if first chr in line.
<> must be included around values and strings.
; must be included to separate parameters.
{ } indicate choose one, and should not be included.
Upper and lower case doesn't matter for function names.
"wait done" is written when script is finished.
For all {on,off} cases, off is set to default.

IMG

IMG BG Make
IMG Sub {on, off}
IMG Avg {on, off}
IMG Image Path {str_name, <C:/Measurements>}
IMG Image Name {str_name, <file name>}
IMG Image Save
IMG Image Mask {opt_str_name, <optional name>}
IMG Video Path {str_name, <C:/Measurements>}
IMG Video Name {str_name, <file name>}
IMG Video REC {on, off}
IMG Comment {str_name, <Short comment>}

MFC

MFC DC {on, off}
MFC AC {on, off}
MFC DECAY {on, off}
MFC INVERT
MFC ZERO
MFC OFFSET {<xx.xx>, iter_name}
MFC DECAY_Time {<seconds>, iter_name}
MFC Rotate_DC {<int>, iter_name}
MFC Rotate_AC {<int>, iter_name}

Log

Log Clear
Log Save {str_name, <C:/Measurements>};{str_name, <name>}
Log Write {str_name, <Comment>}

Miscellaneous:

Iter {a,b,rotate_num,...} {=,+,-,*,/} {<20.40>, iter_name}
String {a,b,rot,...} {=,+} {srn, str_name, <Text>}
String {a,b,rot,...} str iter_name
Wait {<xx.xxx>, iter_name}
For {<#lines>, iter_name};{<#iterations>, iter_name}
Currlne <int>

Updated 28.11.23

A.3 AB ab clocking

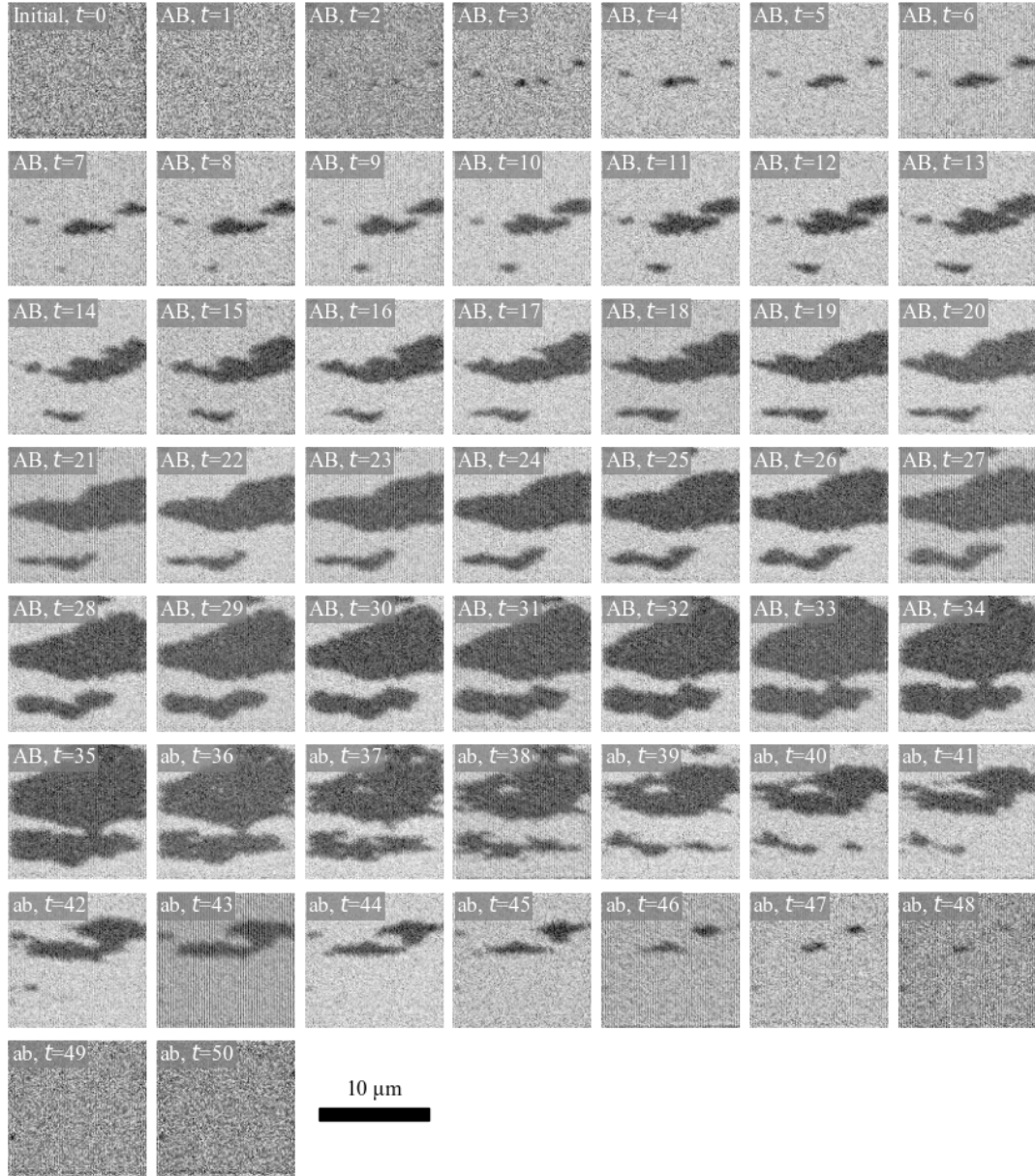


Fig. A.1: Time series on the 11.8 structure using 33 mT trying to optimize the contrast of each images. Minimum and maximum pixel value of each image was used as the minimum and maximum color value. The uniformity of the time series is destroyed by the large variation of extreme point pixel values from one image to the next.

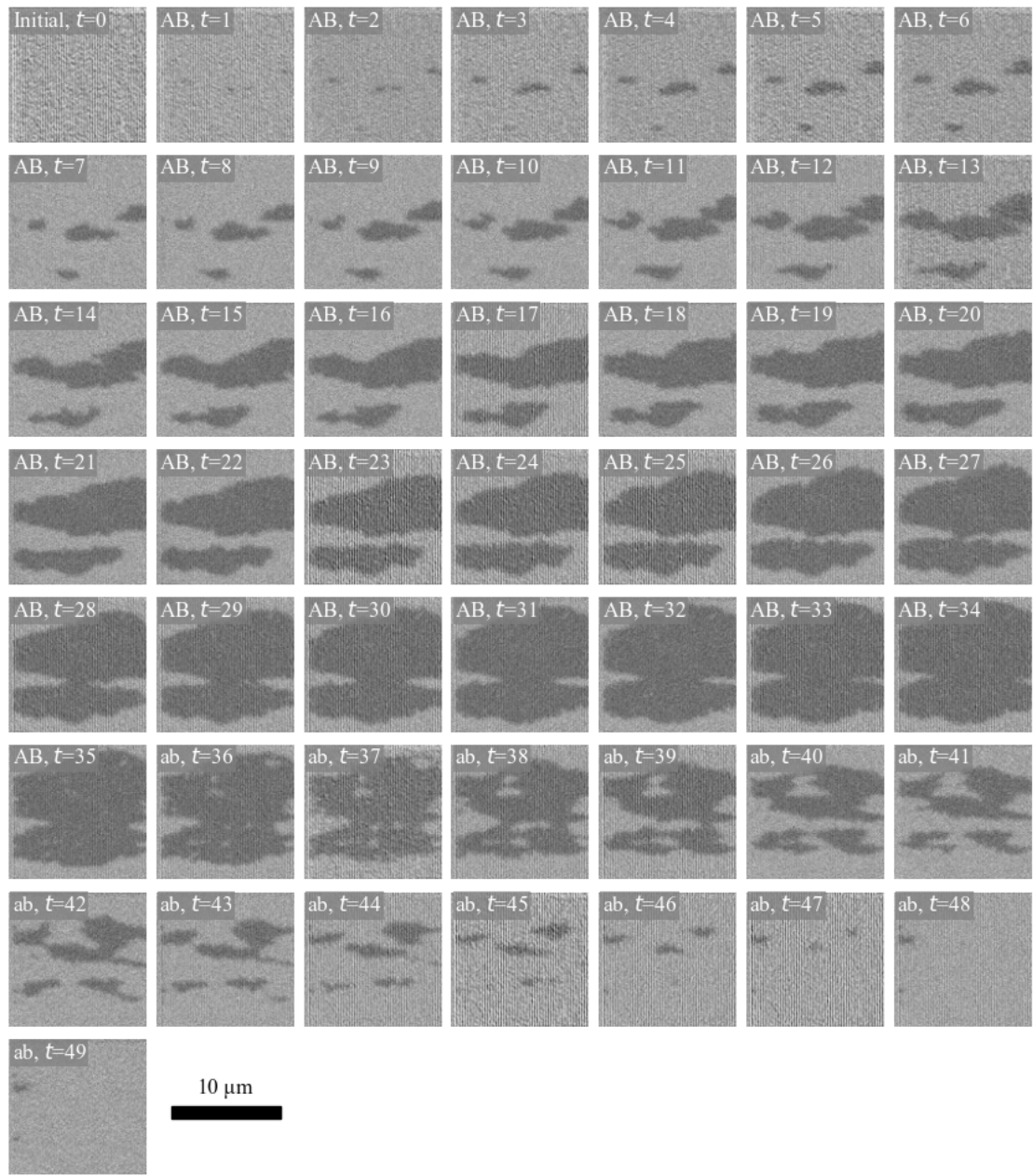


Fig. A.2: Time series on the 11.8 structure using 33 mT for the manual clocking sequence. A lot more noise can be observed compared to the automated sequences.

APPENDIX A. SCRIPTING

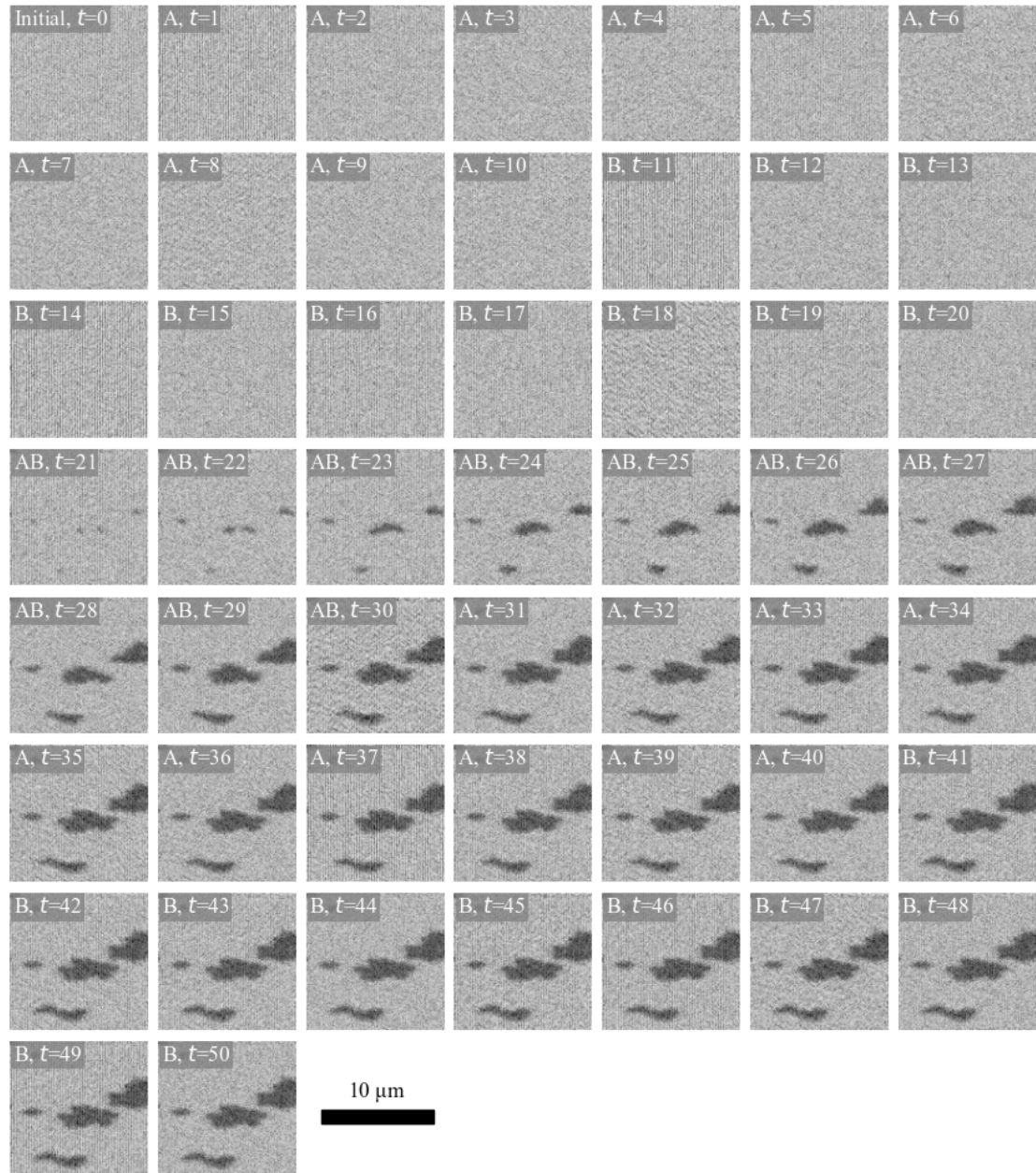


Fig. A.3: Time series on the 11.8 structure using 33 mT, with ten cycles of A-clocking and B-clocking before and after ten AB-cycles.

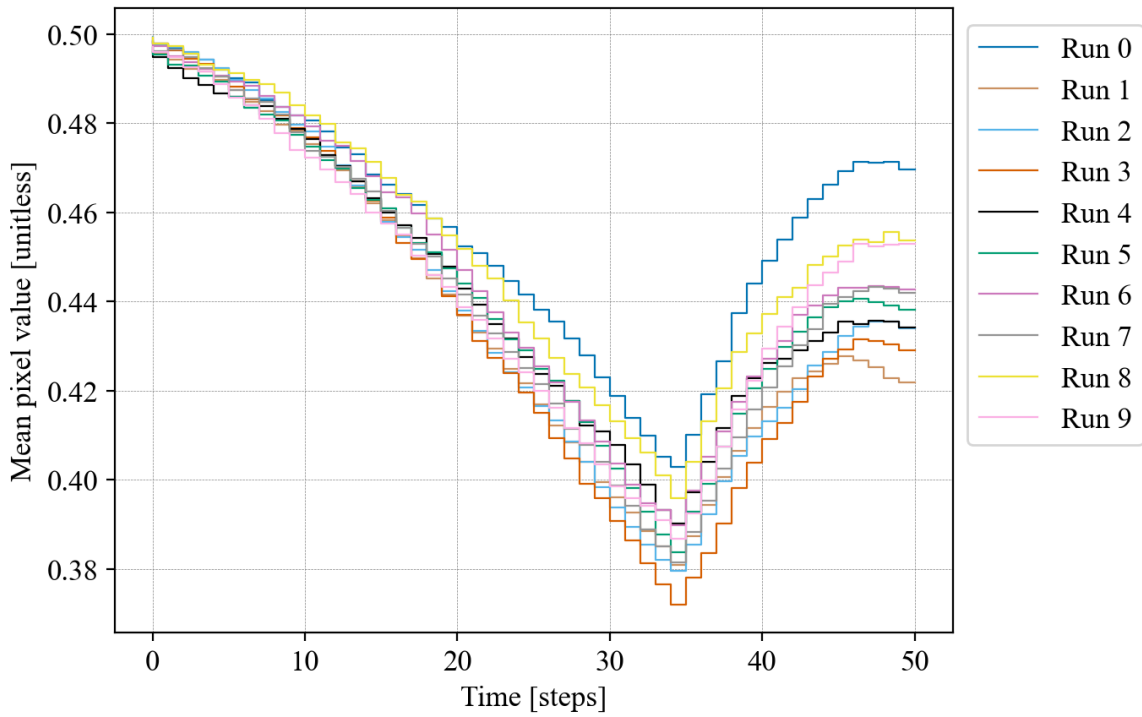


Fig. A.4: Raw intensity plot for the multiple runs.

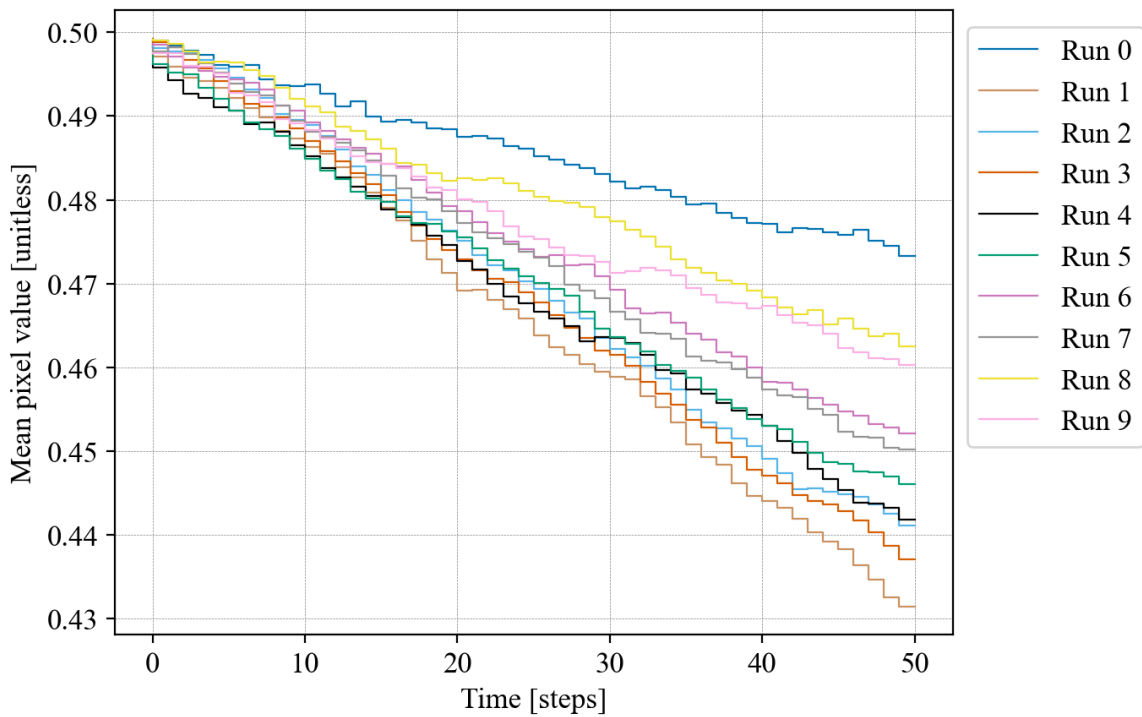


Fig. A.5: Correction intensities for the multiple runs.

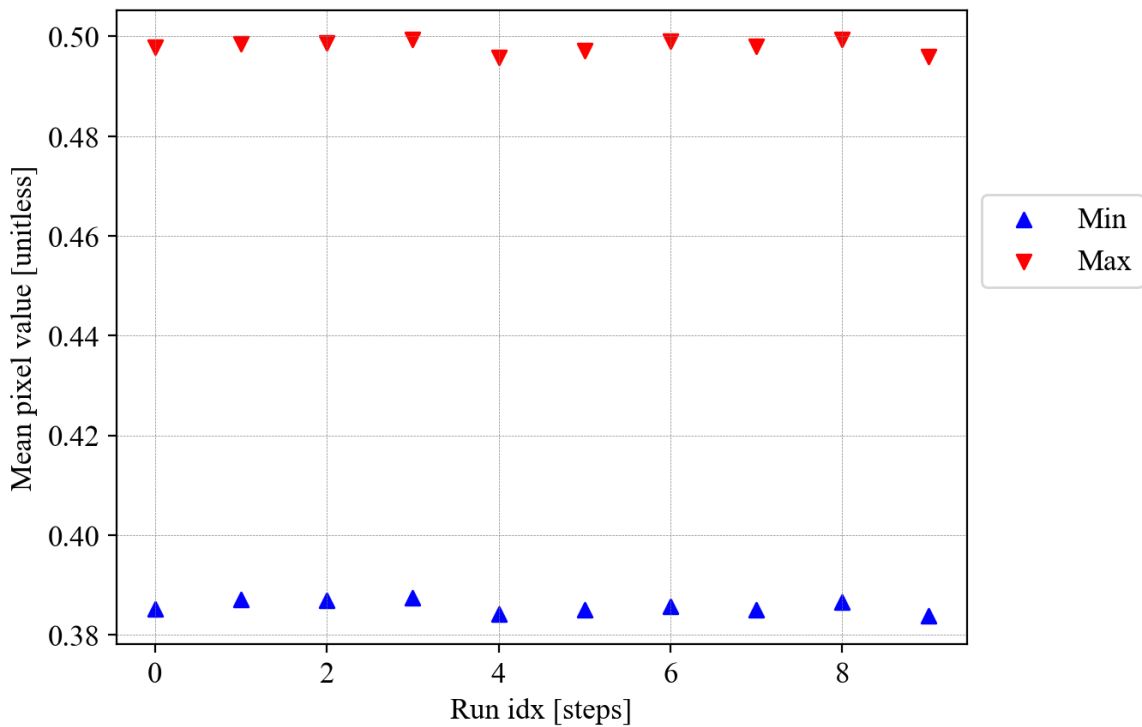


Fig. A.6: Corrected saturation magnetization pixel values for the multiple runs.

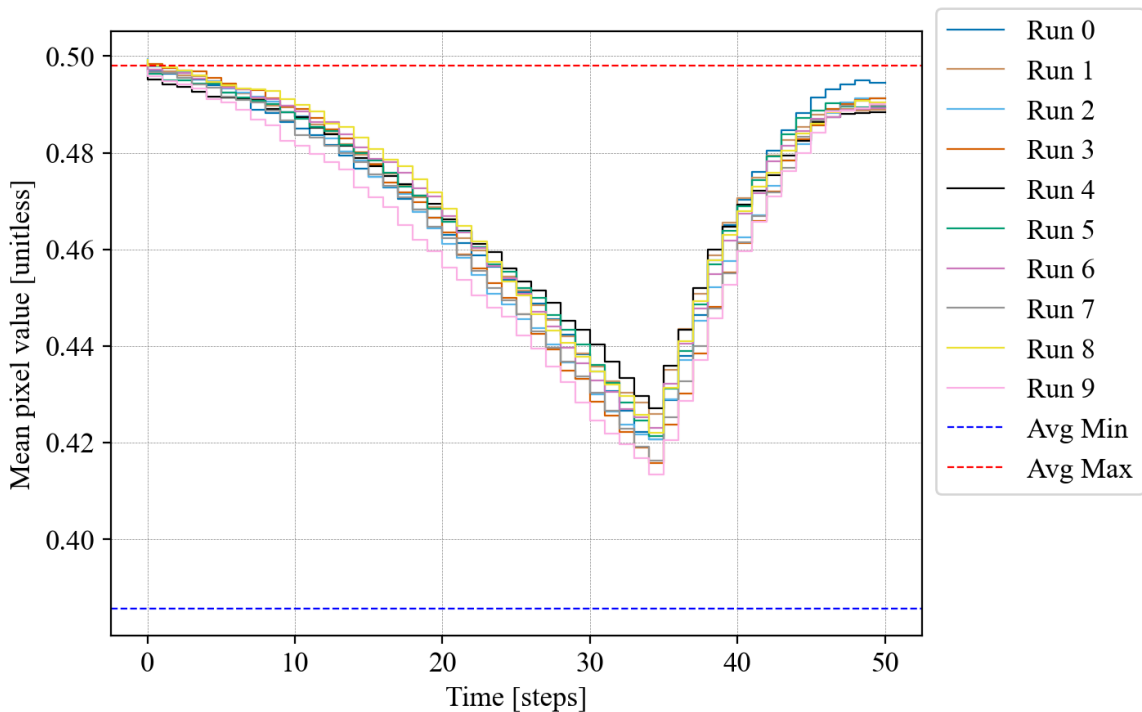


Fig. A.7: Corrected ASI plot for the multiple runs.

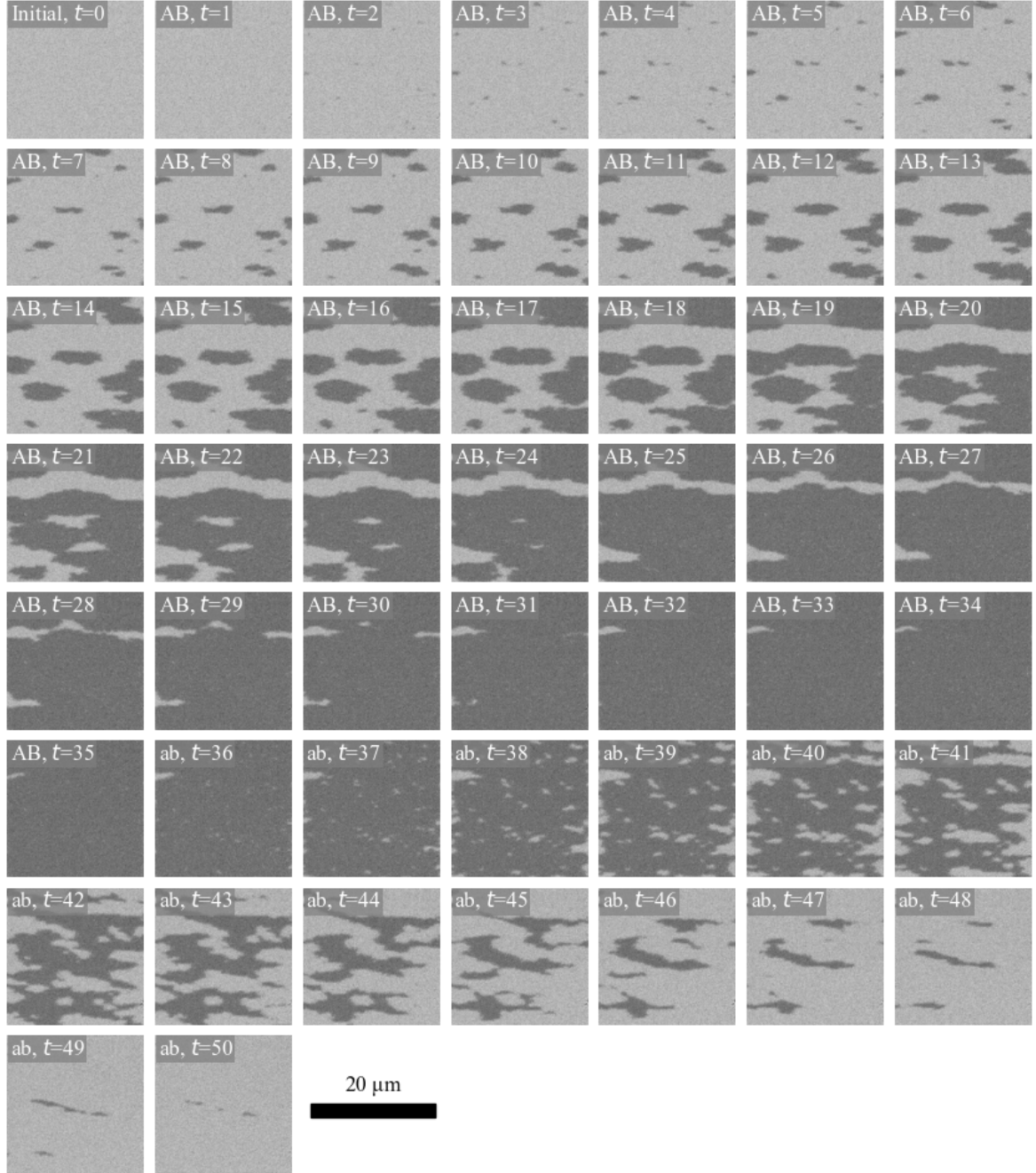


Fig. A.8: Time series on the 12.8 structure using 32 mT. The ASI seems to almost reach the saturation magnetization during AB-clocking.